Supplementary Information (SI) for Journal of Materials Chemistry A.

Supplementary Information

Unveiling the Effect of Structural Asymmetry for Photocatalytic Performance: Bi-substituted $Y_2Sn_2O_7$ System with a Mechanistic Insight

Adarsh Kumar [a, b], Deepak Tyagi [a, b], Ravi Kumar [c], Manasi Ghosh [d], Balaji P. Mandal[a, b], Ahin Roy [e], Sukhendu Nath [b, f], Avesh K. Tyagi* [b], Kaustava Bhattacharyya*[a ,b]

a- *Chemistry Division, Bhabha Atomic Research Centre, Mumbai-40085, India*
b- *Homi Bhabha National Institute, Mumbai - 400 094, India*
c- *Atomic and Molecular Physics Division, Bhabha Atomic Research Centre, Mumbai -400 085, India*
d- *Physics Section, MMV, Banaras Hindu University, Varanasi-221005, India*
e- *Materials Science Centre, Indian Institute of Technology Kharagpur, West Bengal-721302, India*
f- *Radiation and Photochemistry Division, Bhabha Atomic Research Centre, Mumbai-40085, India*

1. Experimental Methods:

In order to reduce the volume of this manuscript the details of the experimental methods are completely described here in the S.I.

A. Characterization

Details of the instrumentation for all the characterization techniques as described in the main manuscript are discussed here.

Phase analysis of crystallography was conducted through powder X-ray diffraction (XRD) measurements using a Phillips Analytical Diffractometer equipped with Ni-filtered Cu Kα radiation. Diffractograms were recorded within the 10-80° (2θ) range, and the average crystallite size was determined using the Williamson Hall's method. UV–visible measurements in the 200–800 nm regions were performed using a two-beam spectrophotometer (V-670, JASCO) with a diffuse reflectance (DR) attachment, employing barium sulphate-coated integration spheres, with $BaSO_4$ as a reference. Laser Raman spectra were acquired on a LABRAM-1 spectrometer (ISA) in back-scattering geometry (Spectral resolution =2 cm^{-1}) using an Ar^+ ion laser (488 nm) as an excitation source. Transmission electron microscope (TEM) data were obtained using a JEOL GRAND-ARM microscope operated at 300 kV equipped with EDS. TEM samples were prepared by dispersing powder ultrasonically in alcohol onto a carbon-coated copper grid, followed by air-drying.

To elucidate the electronic states, X-Ray Photoelectron Spectroscopy (XPS) study was conducted on a SPECS instrument with a PHOBIOS 150 Delay Line Detector (DLD) employing an Mg Kα (1283.6eV) dual anode as X-ray source (power: 385W, Voltage: 13.85 kV, sample current: 175.6 nA) at a pass energy of 50 eV. As an internal reference for the absolute binding energy, the C-1s peak (284.5 eV) was used. All the deconvolutions are made by the CASA software with Voigt type peak having GL (30) without imparting any asymmetry. The baseline was made using the Shirley function. The BET surface area, pore volume, and pore size distribution were determined through physical adsorption of N_2 at 77 K using a Micromeritics ASAP 2020 analyzer, after degassing under vacuum at 300 °C. Zeta potential measurements were performed at 25 °C using a quartz cuvette with a Malvern Zetasizer nanoseries, employing phase analysis light scattering with applied field strength of 2.5×10^3 V/m and a He-Ne laser (632.8 nm) operating at 4.0 mW as the light source. About 0.5 mg/mL of the sample was dispersed in 1 mL of water. In order to understand the different O-vacancies in the structures EPR was conducted using the BRUKER BIOSPIN, Germany, EMXmicro A200-9.5/12/S/W instrument.

X-ray Absorption Spectroscopy (XAS) measurements, encompassing both X-ray Near Edge Structure (XANES) and Extended X-ray Absorption Fine Structure (EXAFS) techniques, were carried out to probe the local structure of $Y_{2-x}Bi_xSn_2O_7$ at Y, Sn K edge, and Bi L_3 edge at the Energy-Scanning EXAFS beam line (BL-9) at the Indus-2 Synchrotron Source (2.5 GeV, 100 mA) at Raja Ramanna Centre for Advanced Technology (RRCAT)[1,2,3,4] Indore, India. The beam line operates in the energy range of 4 KeV to 25 KeV. The beamline optics consists of a Rh/Pt coated collimating meridional cylindrical mirror and the collimated beam reflected by the mirror is monochromatized by a Si (111) (2d=6.2709 Å) based double crystal monochromator (DCM). The second crystal of DCM is a sagittal cylinder used for horizontal focusing while a Rh/Pt coated bendable post mirror facing down is used for vertical focusing of the beam at the sample position. Rejection of the higher harmonics content in the X-ray beam is performed by detuning the second crystal of DCM. In the present case, Bi and Sn edge XAS data have been measured in transmission mode and Y edge data have been measured in fluorescence mode. For the transmission mode measurement, three ionization chambers (300 mm length each) have been used for data collection, one ionization chamber for measuring incident flux (I_0), second one for measuring transmitted flux (I_t) and the third ionization chamber for measuring XAS spectrum of a reference metal foil for energy calibration. Appropriate gas pressure and gas mixtures have been chosen to achieve 10-20% absorption in first ionization chamber and 70-90% absorption in second ionization chamber to improve the signal to noise ratio. The absorption coefficient μ is obtained using the relation:

a. $I_T = I_0 e^{-\mu x}$ ……………………………………(1)

Where, x is the thickness of the absorber.

For measurements in the fluorescence mode, the sample is placed at 45°to the incident X-ray beam, and a fluorescence detector is placed at right angle to the incident X-ray beam to collect the signal. One ionization chamber detector is placed prior to the sample to measure the incident flux (I_0) and florescence detector measures the fluorescence intensity (I_f). In this case the X-ray absorption co-efficient of the sample is determined by $\mu = I_f / I_0$, and the spectrum was obtained as a function of energy by scanning the monochromator over the specified range

The XAS data acquired as above are analysed flowing standard procedure[3]. In brief to obtain the qualitative information about the local structure, oscillations in the absorption spectra $\mu(E)$ have been converted to absorption function $\chi(E)$ defined as follows:

$$\chi(E) = \frac{\mu(E) - \mu_0(E)}{\Delta\mu_0(E_0)}$$

………………………………………………(2)

where, E_0 is absorption edge energy, $\mu_0(E_0)$ is the bare atom background and $\Delta\mu_0(E_0)$ is the step in $\mu(E)$ value at the absorption edge. The energy dependent absorption coefficient $\chi(E)$ has been converted to the wave number dependent absorption coefficient $\chi(k)$ using the relation,

b. $K = \sqrt{\frac{2m(E - E_0)}{\hbar^2}}$ …………… (3)

Where, m is the electron mass. $\chi(k)$ is weighted byk^2 to amplify the oscillation at high k and the$\chi(k)k^2$ functions are fourier transformed in R space to generate the $\chi(R)$ versus R plots in terms of the real distances from the center of the absorbing atom. Subsequently theoretical versus R plots are generated assuming possible crystal structure of the sample and are fitted with the experimental data to determine the local structural parameters. [1, 2, 3]

The set of EXAFS data analysis programme available within Demeter [4] software **package** have been used for EXAFS data analysis. This includes background reduction and Fourier transform to derive the $\chi(R)$ versus R spectra from the absorption spectra (using ATHENA[3] software), generation of the theoretical EXAFS spectra starting from an assumed crystallographic structure and finally fitting of experimental data with the theoretical spectra using ARTEMIS [3] software.

The goodness of fit has been determined by the value of the R_{factor} defined by:

$$R_{factor} = \sum \frac{[\mathrm{Im}(\chi_{dat}(r_i) - \chi_{th}(r_i)]^2 + [\mathrm{Re}(\chi_{dat}(r_i) - \chi_{th}(r_i)]^2}{[\mathrm{Im}(\chi_{dat}(r_i)]^2 + [\mathrm{Re}(\chi_{dat}(r_i)]^2} \qquad \text{………… (4)}$$

where, χ_{dat} and χ_{th} refer to the experimental and theoretical $\chi(r)$ values respectively and 'Im' and 'Re' refer to the imaginary and real parts of the respective quantities.

B. Photo-electrochemical measurements:

P-type Silicon (1 0 0) wafers (Cleaned with piranha solution with resistivity range-1 to 10 Ω cm), were used as substrates to disperse $Y_{2-x}Bi_xSn_2O_7$ drop casts. Drop casting method for dispersing $Y_{2-x}Bi_xSn_2O_7$ samples over Si (1 0 0) substrate. In a typical procedure, 100 mg of the catalyst ($Y_{2-x}Bi_xSn_2O_7$) was dispersed in 1 mL isopropanol, supplemented with 30 μL of Nafion (binder), and subjected to ultra-sonication for 30 minutes to ensure a homogeneous dispersion. The resulting supernatant from the dispersion was drop-cast onto the substrate surface. Following even coating, the substrate underwent a drying process at 60 ºC for 2 hours. An electrochemical cell was assembled utilizing Si/$Y_{2-x}Bi_xSn_2O_7$ as the working electrode, a platinum wire coil as the counter electrode, and a platinum wire as the pseudo reference electrode. The electrolyte employed in the experiment was 0.1M KCl. The electrochemical cell was connected to the Potentiostat/Galvanostat PARSTAT-2273 for chrono-amperometric switching studies at a bias of -1.5V. The cell was irradiated with 1.5 AM sunlight-type radiation from the Optosolar cell testing system.

C. *Ex-Situ* FT-IR

In this study, we conducted an experimental analysis on $Bi_{2-x}Y_xSn_2O_7$ (x = 0 -2.0) pyrochlores to compare their photocatalytic activity for the oxidation of para-chloro phenol (p-CP). This investigation is essential for understanding the reaction kinetics and identifying different intermediates formed during the oxidation of p-CP, leading to the production of carbon dioxide, using a diverse set of catalysts (details in S.I.). For the ex-situ FT-IR study, a 60 cc p-CP aqueous solution with a molar concentration of 0.14 moles/l was placed in a beaker, and each pyrochlore photocatalyst (100 mg) was added. The photocatalytic system was initially stirred for 20 min at 200 rpm in the dark to disperse the powders for adsorption analysis. Subsequently, the systems were exposed to visible light. At 10-minute intervals, a drop of the sample was added to a KBr pellet, and corresponding peaks were measured using an ex-situ-IR instrument. The same stirring procedure was repeated for the other mixtures, with IR peaks measured after 10 minutes of stirring. Notably, complete degradation of p-CP was observed in ~ 60 minutes when utilizing $Bi_2Sn_2O_7$ as the catalyst, while for other catalysts ($Y_{0.4}Bi_{1.6}Sn_2O_7$, $Y_{0.3}Bi_{1.7}Sn_2O_7$, $Y_{0.2}Bi_{1.8}Sn_2O_7$ and $Y_2Sn_2O_7$), complete degradation of p-CP occurred in ~ 120 to 180 minutes. The study initially involved testing by acquiring FT-IR spectra of p-CP in a liquid cell. A drop of p-CP aqueous solution, utilized in photocatalytic reactions, was taken to understand the effective spectra with a KBr pellet (Fig.S-7). Notably, all bands were generally similar, except for the band at 1640 cm^{-1}, representing the bending vibration of H_2O. This discrepancy arises from the presence of H_2O in the p-CP solution, as indicated by the broad band at 3350 cm^{-1}, encapsulating the stretch band of the H_2O moiety over KBr. A single KBr pellet was utilized for FT-IR spectra at a specific time during the reaction and then discarded. This practice ensured that different IR spectra resembled those of the intermediates of p-CP formed during the photo-oxidation reaction over time, with minimal or no interaction with the KBr pellet observed for both intermediates and the initial p-CP.

D. Femtosecond Transient Absorption (FTAS) and Time Resolved Photoluminescence Experiments (TRPL).

Time-resolved photoluminescence (TRPL) was measured using a time-correlated single photon counting spectrofluorometer (IBH, UK) with a 375 nm diode laser excitation and detection at the emission maximum. The instrument response function was 0.22 ns, and measurements were performed under magic angle polarization. Femtosecond transient absorption (TA) was performed using a CDP Corporation pump-probe setup from CDP Corporation, Moscow, following established protocols. A 350 nm pump pulse, generated from an 800 nm Ti-sapphire laser (Amplitude Technologies, France) via an optical parametric amplifier and BBO crystals, excited the sample. A broadband white light (350-1100 nm) probe pulse, generated by focusing a portion of the 800 nm laser on a rotating CaF_2 disk, monitored the resulting transient species. A CDP Corporation diode array detector recorded the probe pulse. Transient absorption spectra were acquired at various pump-probe delays and averaged over at least two runs. The 1 mm optical cell containing the sample was rotated to prevent degradation.

2. Self- Degradation of P-CP in visible and UV irradiation

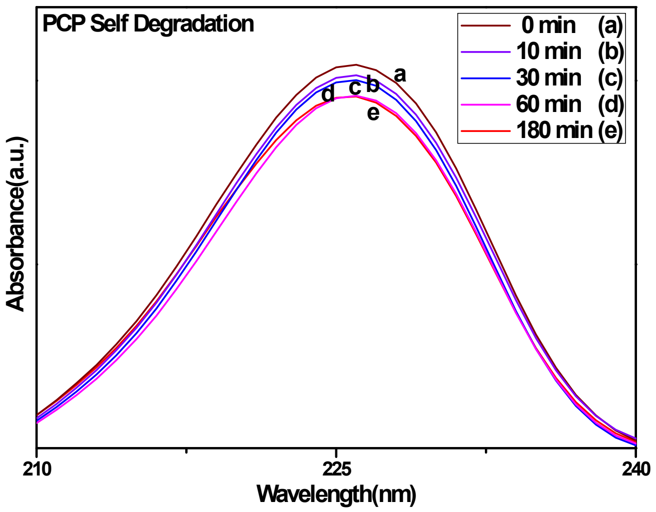

S-1(a): UV -Vis data for self- degradation of p-CP in Visible light irradiation

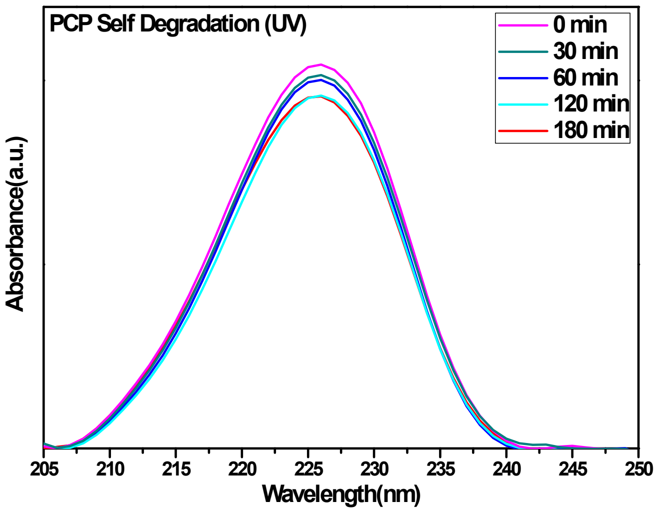

S-1.(b): UV -Vis data for self- degradation of p-CP in UV-light irradiation

3. Photocatalytic Activity with Visible and UV -irradiation

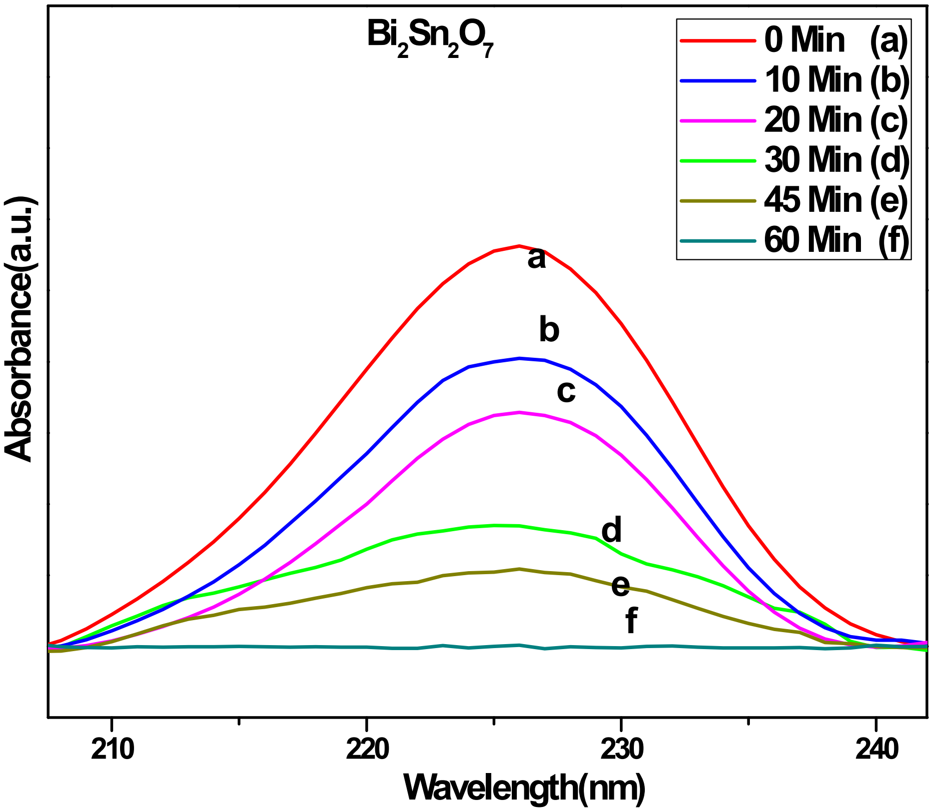

Fig.S-2: Degradation of p-CP using $Bi_2Sn_2O_7$ photocatalyst as a function of time: a) 0 min; b) 10 min; c) 20 min; d) 30 min; e) 45 min; f) 60 min.

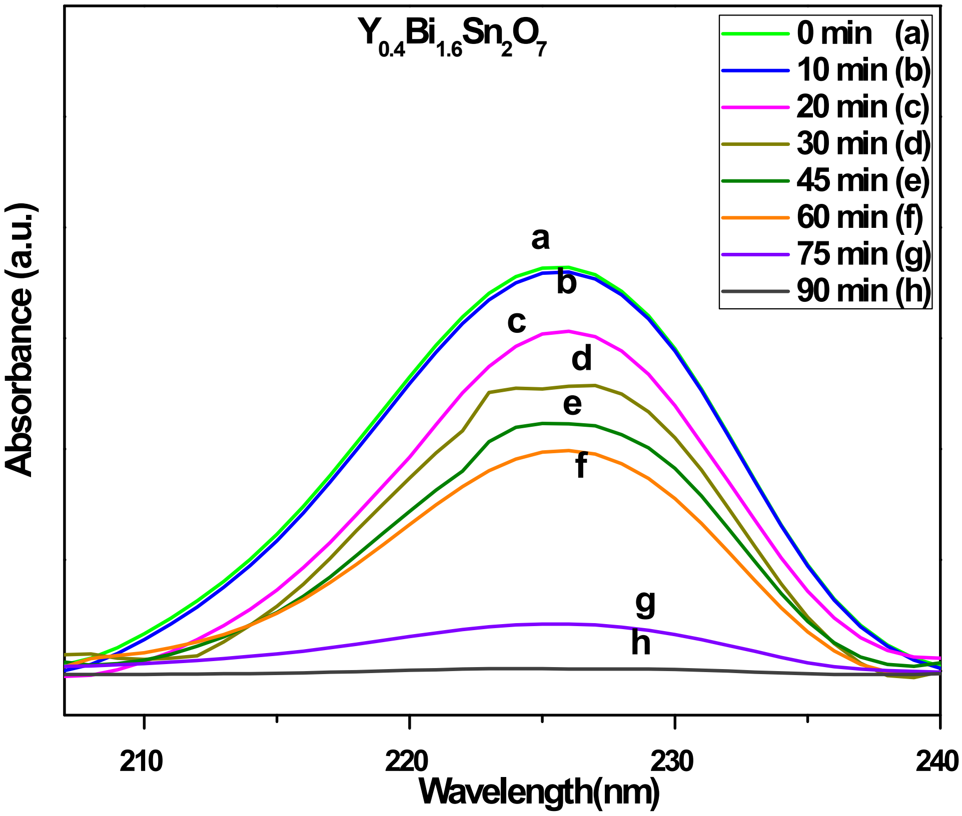

Fig.S-3: Degradation of p-CP using $Y_{0.1}Bi_{1.9}Sn_2O_7$ photocatalyst as a function of time: a) 0 min; b) 10 min; c) 20 min; d) 30 min; e) 45 min; f) 60 min; g) 75 min; h) 90 min.

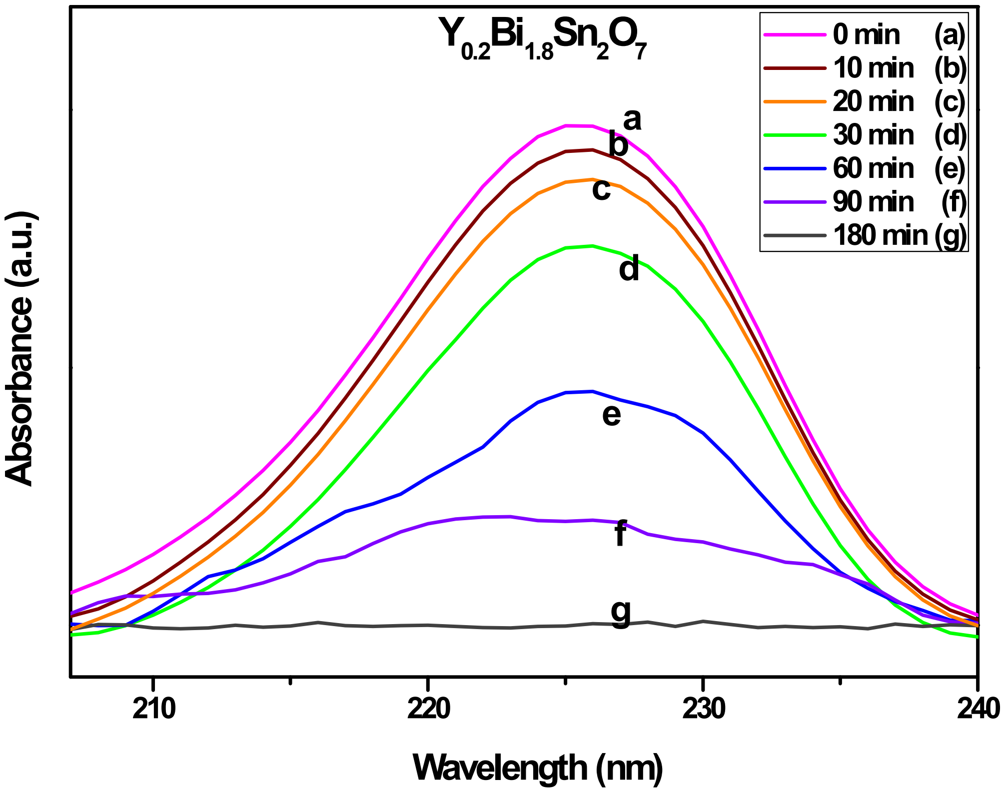

Fig.S-4: Degradation of p-CP using $Y_{0.2}Bi_{1.8}Sn_2O_7$ photocatalyst as a function of time: a) 0 min; b) 10 min; c) 20 min; d) 30 min; e) 60 min; f) 90 min; g) 120 min.

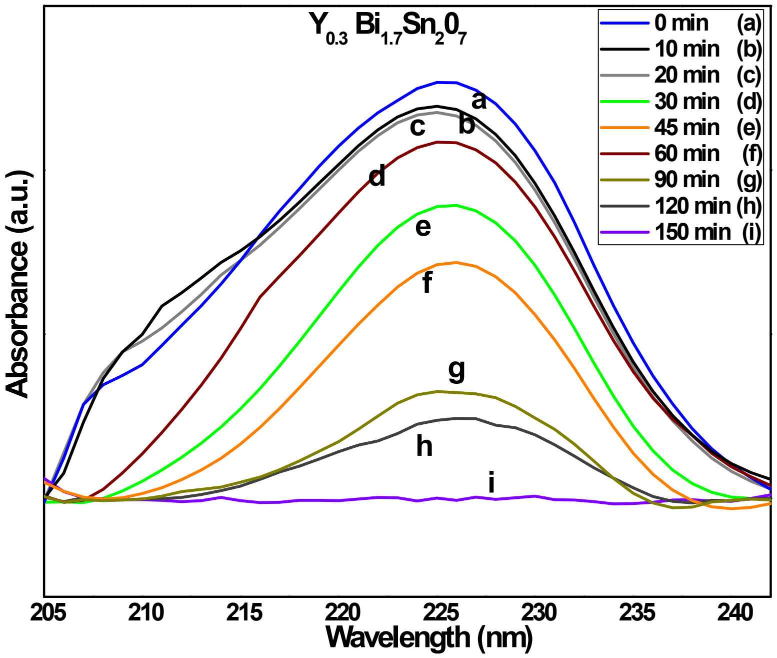

Fig.S-5: Degradation of p-CP using $Y_{0.3}Bi_{1.7}Sn_2O_7$ photocatalyst as a function of time: a) 0 min; b) 10 min; c) 20 min; d) 30 min; e) 45 min; f) 60 min; g) 90 min; h) 120 min; i) 150 min.

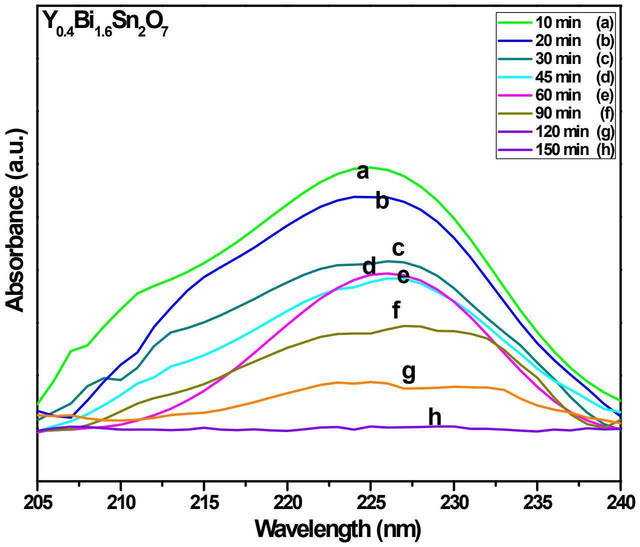

Fig.S-6: Degradation of p-CP using $Y_{0.4}Bi_{1.6}Sn_2O_7$ photocatalyst as a function of time: a) 10 min; b) 20 min; c) 30 min; d) 45 min; e) 60 min; f) 90min; g) 120 min; h) 150 min.

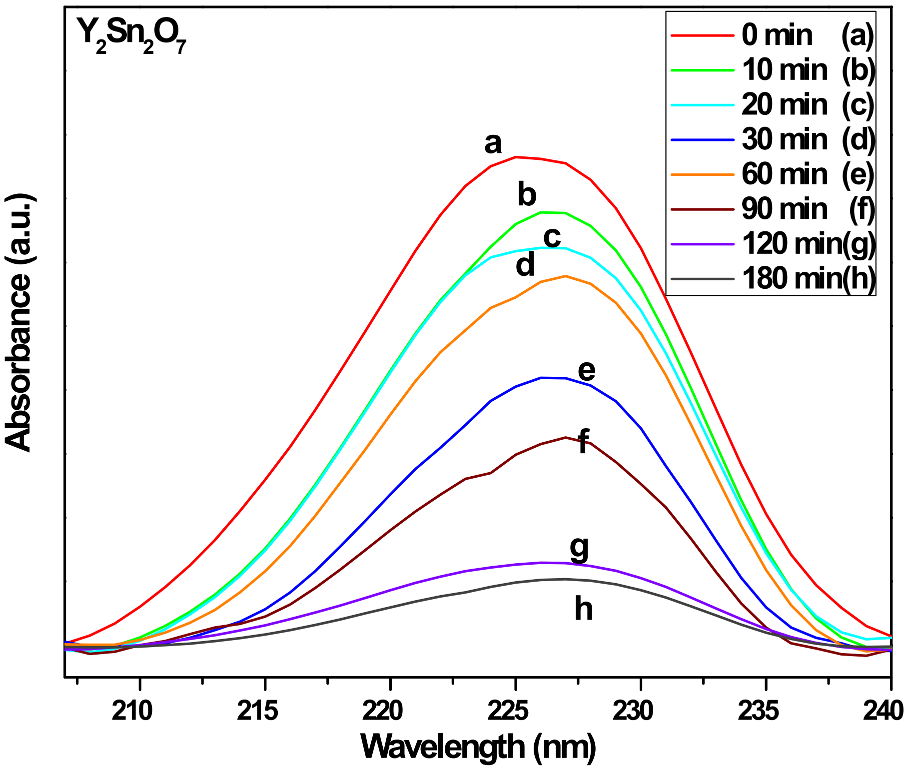

Fig.S-7: Degradation of p-CP using $Y_2Sn_2O_7$ photocatalyst as a function of time: a) 0 min; b) 10 min; c) 20 min; d) 30 min; e) 60 min; f) 90 min; g) 120 min; h) 180 min.

4. Understanding the adsorption of p-CP over different catalysts.

1) p-CP adsorption

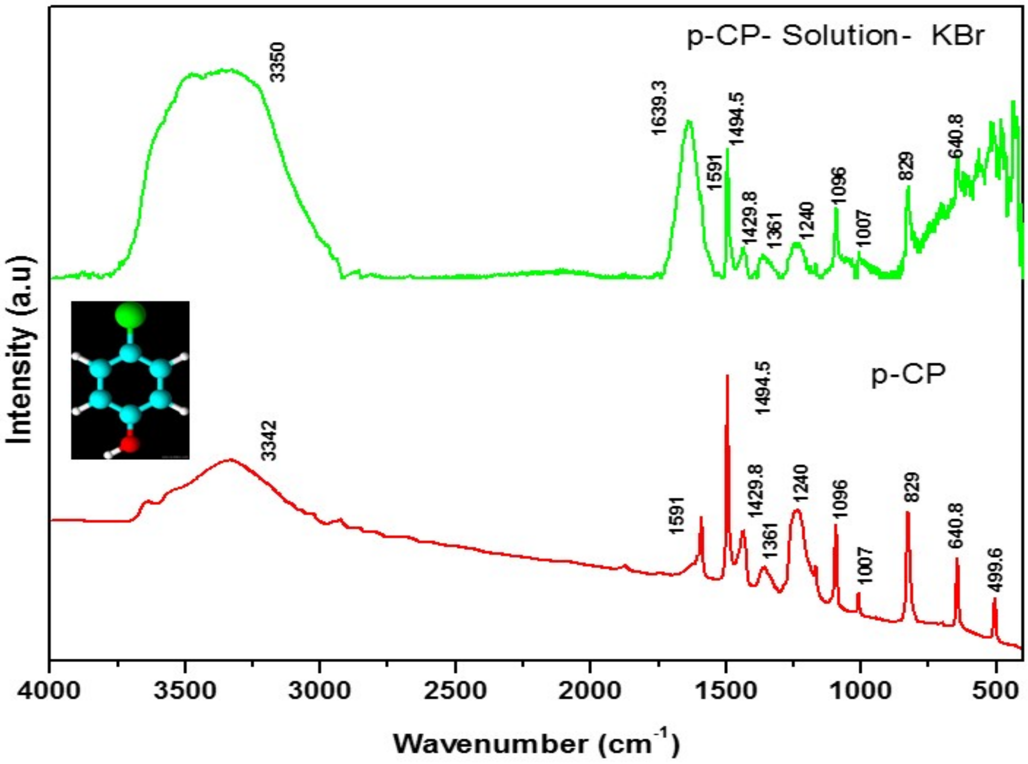

Fig. S.8: (A) p-CP over KBr and (B) IR data of liquid p-CP sample.

The Fig. S-8.(B) shows the FT-IR bands for the p-CP as given in the Fig.6.B and below table labels the assignment for the p-Chloro phenol as has been assigned previously in the literature.

Serial No	FT-IR bands (cm^{-1})	Assignments	Reference
1	3342	ν- OH- Stretch	-
2	1591	ν-CH ; *ν*(C3-C4) -Structural -Ph and C-H	5, 6
3	1494	ν (C-C), *δ*-CH, *δ*-OH	7, 8 , 9
4	1429.8	ν (C-C) *δ*-OH	-
5	1361	ν (C-C), *δ*-CH, *δ*-OH	10
6	1240	*ν*(C-O), *δ*(C-C), *δ*CH	11, 12
7	1096	*ν* (C4-C5); *ν* (C3-C4), *ν* (C-Cl)	13, 14
8	1007	*δ*-ring, *ν* (C-C), *δ* CH	6, 15, 16
9	829	*γ*-C6-H, *γ*-C5-H, *γ*-CO	8, 17, 18
10	640.8	*γ* CO, *τ*3ring, *γ* -CCl	8, 13, 19
11	500	*δ* CO, *δ* 3ring, *δ* CCl	6, 20, 21

Table-S-1: Assignment of the different bands for p-CP.

The Fig.S-7.A shows the different peak of the FT-IR that is obtained upon taking IR of p-CP solution over KBr. The additional band of 1630 cm^{-1} is for the H-O- H bend and the other band apart from 3350 cm^{-1} signifies the stretch of H-OH. All the bands as found in the Fig.S-7 (A, B) are assigned in the above table.

The phenomenon of adsorption described below is that of p-CP solution over the solvated photocatalyst. Here the IR spectra over the KBr pellet for the p-CP solution and the p-CP solution with the photocatalyst is compared and it is assumed that the next one shows the intermediates formed with the photo-catalyst. Here the data is taken in dark and without any irradiation just to understand the adsorption behaviour of p-CP solution over the different catalysts.

4.a. Adsorption of p-CP over $Y_2Sn_2O_7$ Surface

The below fig. S.8 shows the IR spectra for p-CP solution and the same after adsorption of p-CP over $Y_2Sn_2O_7$. The new vibrational bands are obtained as triplet (2967, 2924 and 2855) cm^{-1} which suggests formation of enolates.

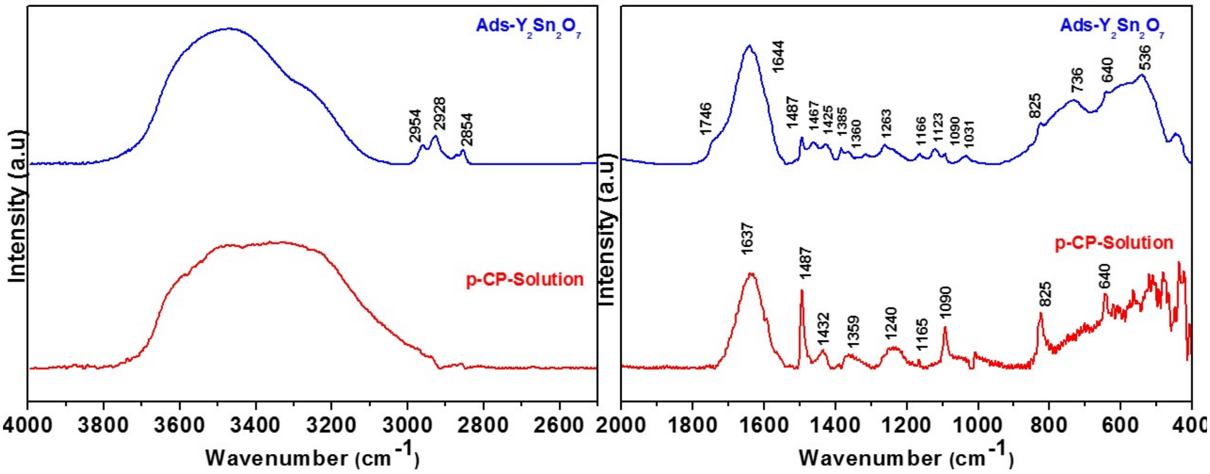

S-9: FT-IR spectra for adsorption of p-CP over $Y_2Sn_2O_7$ photocatalyst in the vibrational range; a) (4000- 2500) cm^{-1}; B) (2400-400) cm^{-1} showing samples for a) p-CP -solution; b) adsorbed p-CP over $Y_2Sn_2O_7$.

The presence of the triplet strong bands at 2985, 2927 and 2972 cm^{-1} has been previously seen as the >C=C<, C-H for adsorbed o-DCB in the "enolic form" over the CeO_2-TiO_2 catalytic surface previously by Wang *et al* [5]. Other new vibrational bands are obtained at a shoulder at 1746 cm^{-1}, doublet at (1467, 1425) cm^{-1} is also for the C-H stretch of the enolates [22, 23] the bands at (1385, 1263, 1123, 1031) cm^{-1}- the bands at 1263 and 1385 cm^{-1} represents the C=C stretch of phenolates and the bands at 1123 and 1031 cm^{-1} represents that of the C- H stretch of enolates. The other noticeable part is the vibrational bands representing the C-Cl (1096, 640.8, 500) cm^{-1} has been weakened considerably mostly prompting cleavage of C-Cl bond. Therefore, the above discussion concludes that the Ph-Cl and Ph-OH bond together results to form the enolates over the $Y_2Sn_2O_7$ surface. The adsorbate being p-chlorophenol the enolate may not be that stable which may still form the phenolates again.

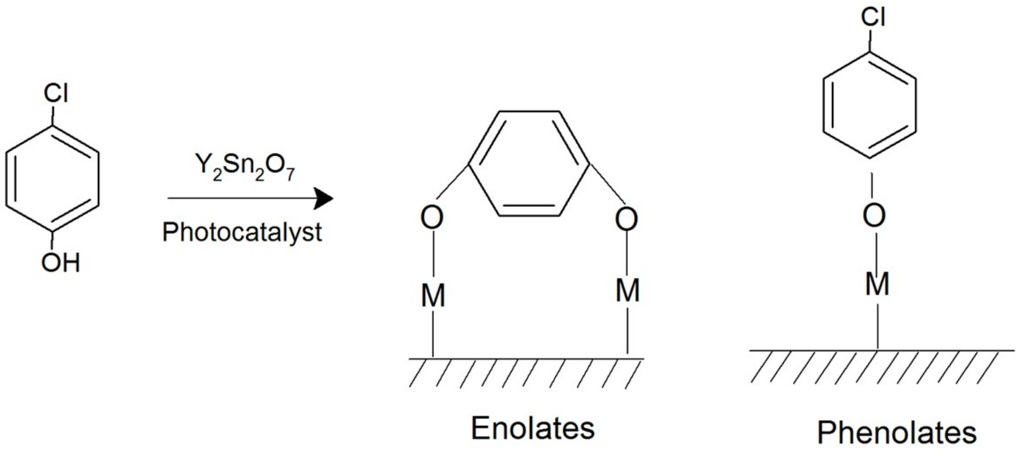

Scheme-1: Adsorption of p-CP over $Y_2Sn_2O_7$ photocatalysts

4.b. Adsorption of p-CP over $Bi_2Sn_2O_7$ Surface

All other peaks are similar as that of the p-CP solution as has been portrayed in the Fig. S-9.

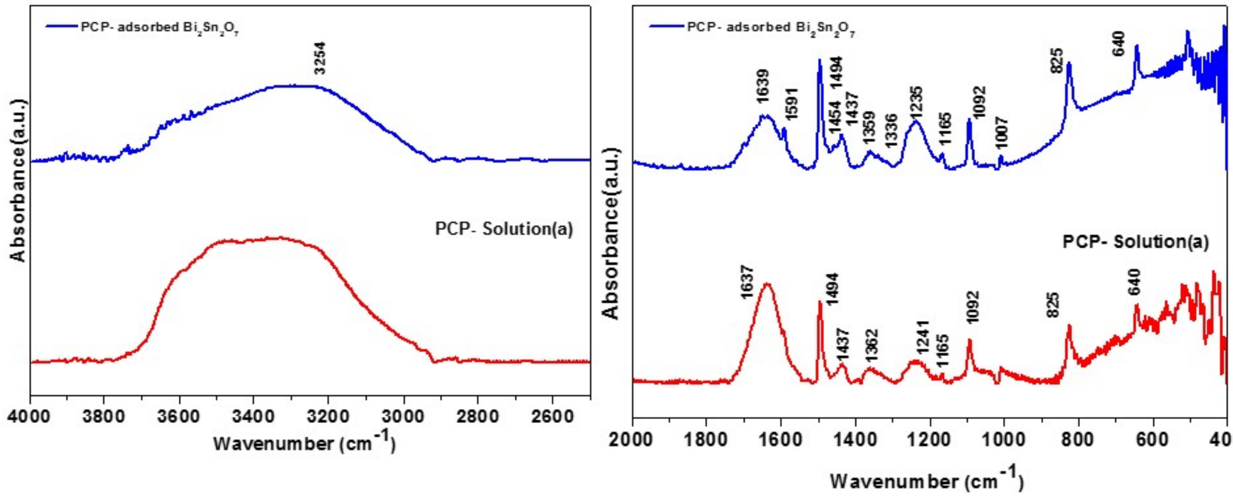

S-10: FT-IR spectra for adsorption of p-CP over $Bi_2Sn_2O_7$ photocatalyst in the vibrational range; a) (4000- 2500) cm^{-1}; B) (2500-400) cm^{-1} showing samples for a) p-CP -solution; b) adsorbed p-CP over $Bi_2Sn_2O_7$.

The peak at 1494cm^{-1} increases in intensity with a new peak at 1594 cm^{-1}and a shift in the peak at 1639 cm^{-1}. All other peaks are same as that of p-CP solution. The new peaks are obtained at (1642, 1591 and 1494) cm^{-1} are denoted for the π-ring complex adsorbed over V_2O_5-TiO_2 sample.[24] [25]

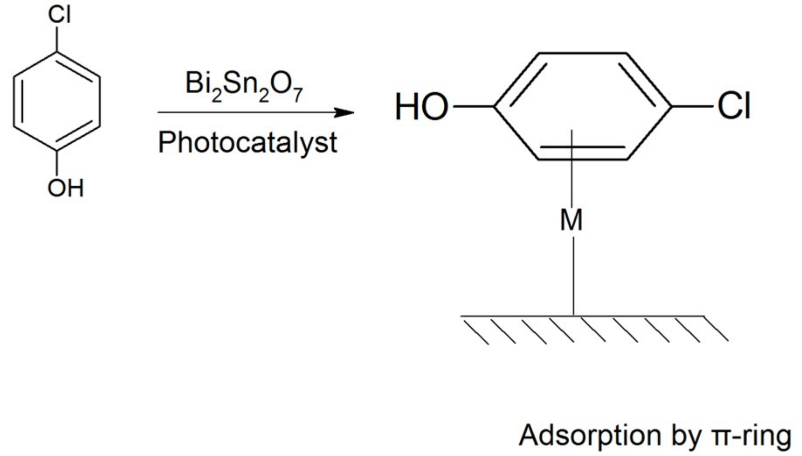

Scheme-2: Adsorption of p-CP over $Bi_2Sn_2O_7$ photocatalysts

4.c Adsorption of p-CP over $Y_{0.4}Bi_{1.6}Sn_2O_7$ -Surface

The below fig. S.8 shows the IR spectra for p-CP solution and the same after adsorption of p-CP over $Y_{0.4}Bi_{1.6}Sn_2O_7$. There are certain negative bands found at (3461, 1634 and 1017) cm^{-1}.

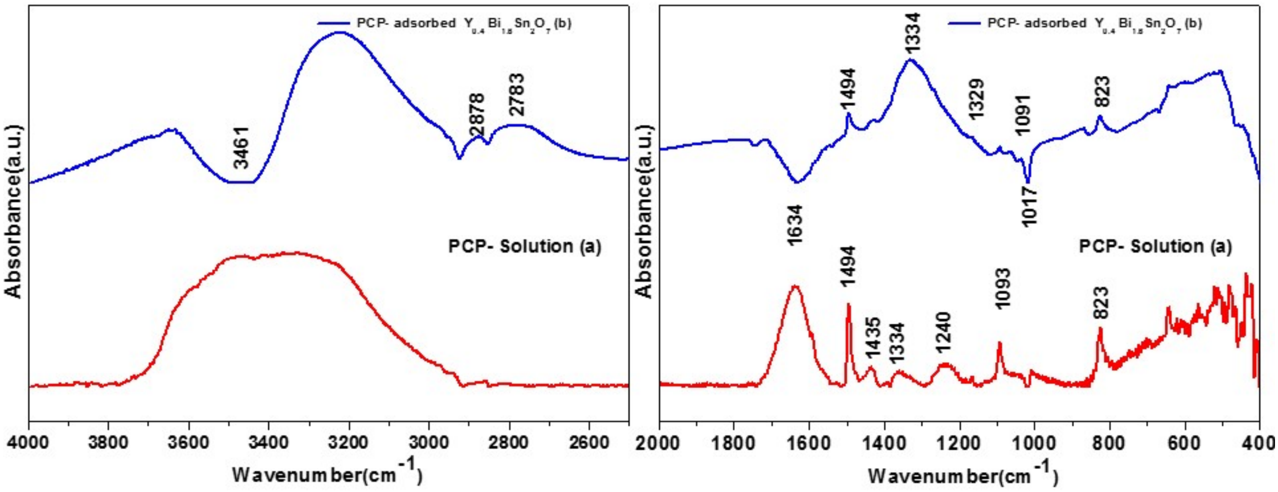

S-11: FT-IR spectra for adsorption of p-CP over $Y_{0.4}Bi_{1.6}Sn_2O_7$ photocatalyst in the vibrational range; a) (4000- 2500) cm-1; B) (2500-400) cm-1 showing samples for a) p-CP -solution; b) adsorbed p-CP over $Y_{0.4}Bi_{1.6}Sn_2O_7$.

They signify usage of the surface hydroxyl group of $Y_{0.4}Bi_{1.6}Sn_2O_7$ -Surface. the new broad band at 1334 cm^{-1} shows formation of phenolates as intermediates as is seen over V_2O_5-CeO_2 catalytic surface earlier by Li et al.[26, 27] However, other vibrational bands representing the C-Cl (1096, 640.8, 500) cm^{-1} remains intact. Therefore, p-CP is adsorbed mainly as the chloro phenolate over the Bi-substituted $Y_2Sn_2O_7$ surface which is completely different from both $Bi_2Sn_2O_7$ and $Y_2Sn_2O_7$ surface as represented in the below Scheme-3.

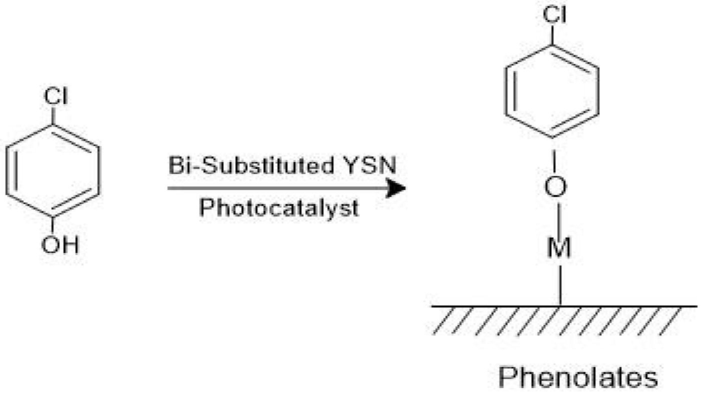

Scheme-3: Adsorption of p-CP over Bi-substituted YSN ($Y_{0.4}Bi_{1.6}Sn_2O_7$) photocatalysts.

5. XPS of Photocatalysts- Y-3p

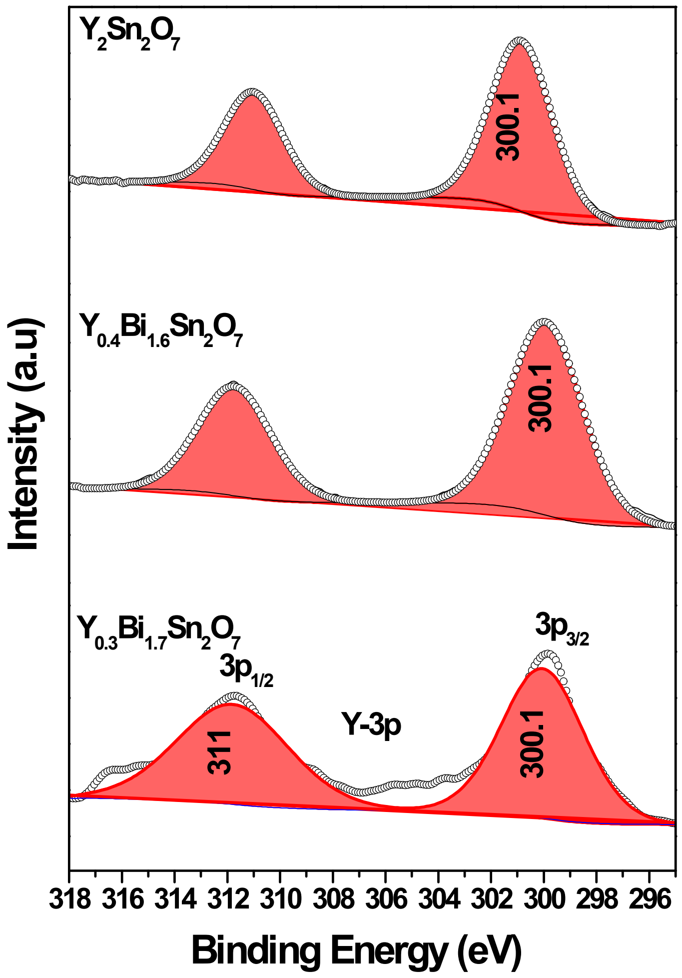

Fig. S-12: XPS figure for Y-3p with deconvolution into $3p_{3/2}$ and $3p_{1/2}$ for different samples: a) $Y_2Sn_2O_7$; b) $Y_{0.4}Bi_{1.6}Sn_2O_7$; c) $Y_{0.3}Bi_{1.7}Sn_2O_7$.

6. EXAFS-Data

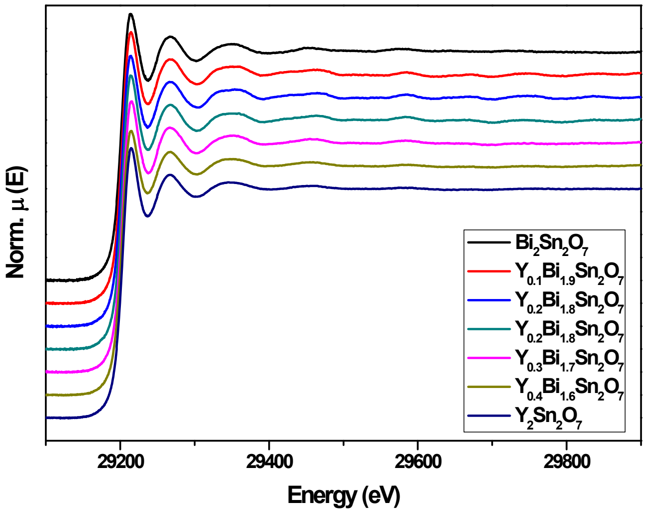

Figure S-13: Normalized XAS spectra of $Y_{2-x}Bi_xSn_2O_7$ samples at Sn K edg

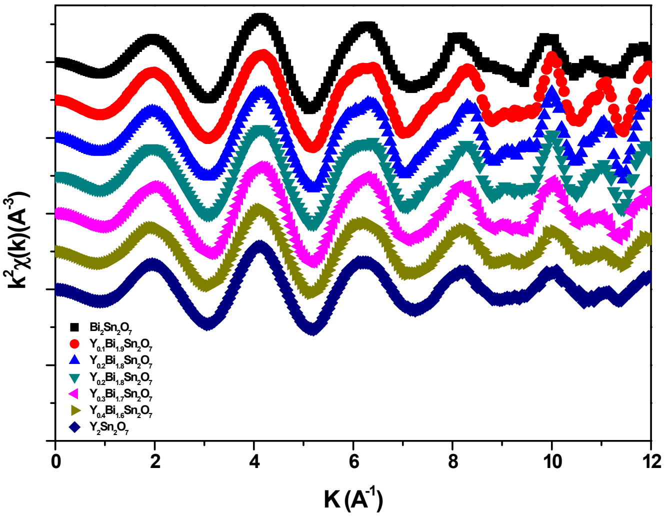

Figure S-14: EXAFS ($k^2\chi$(k) Vs k) spectra of $Y_{2-x}Bi_xSn_2O_7$ samples at Sn K edge.

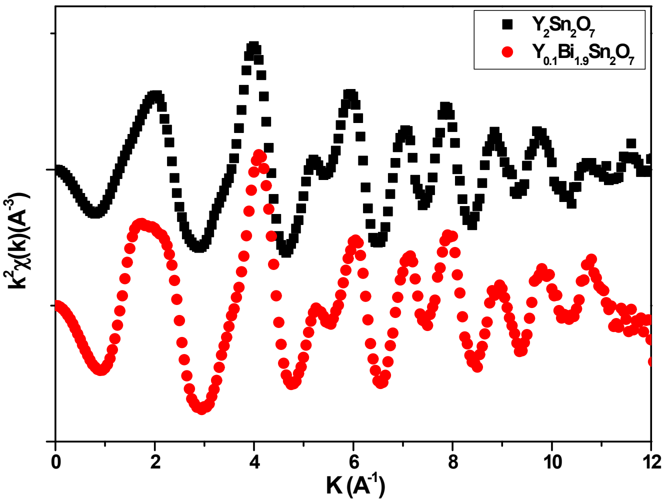

Figure S-15: EXAFS ($k^2\chi$(k) Vs k) spectra of $Y_{2-x}Bi_xSn_2O_7$ samples at Y K edge.

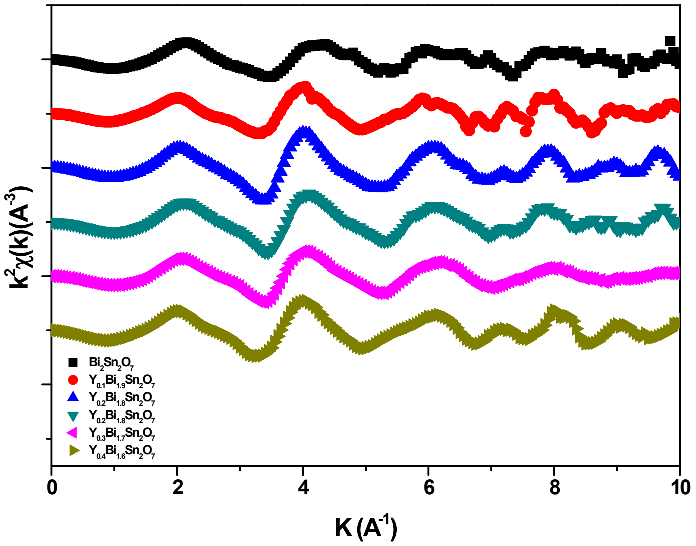

Figure S-16: EXAFS ($k^2\chi$(k) Vs k) spectra of $Y_{2-x}Bi_xSn_2O_7$ samples at Bi L_3 edge.

7. Apparent Quantum Efficiency (AQE) calculation Bi-substituted $Y_2Sn_2O_7$ photocatalysts

AQE of $Y_2Sn_2O_7$

Apparent quantum Efficiency (AQE) is defined as the ratio of number of reacted electrons to the number of incident photons. The general equation is given as below (1, 2, 3, 4)

$$\mathrm{AQE} = \frac{Number\ of\ reacted\ electrons}{Number\ of\ incident\ photons} \times 100 \qquad \text{.............................. (5)}$$

As given in equation (1), during the photocatalytic p-CP oxidation, stoichimetrically 2, electrons are required to produce one molecule of CO2. Though this reaction is a multistep reaction and to be checked which is the slowest, however generically each step being a 2 eletron step will mostly a two electron step.

$$3C_6H_5OCl + 39/2\ O_2 \longrightarrow 18\ CO_2 + 6\ H_2O + 3HCl \qquad \text{........................ (6)}$$

Therefore, number of reacted electrons can be calculated by directly multiplying 2 with mole of CO_2 produced during the photocatalytic reaction.

$$\text{Number of reacted electrons} = [P.F] \times 2 \times N_A \qquad \text{.............................. (7)}$$

Where, [P.F] = Percent Product fomed from $3.3\mathrm{x}10^{-5}$ Molar solution in time (*t*) & N_A = Avogadro's number (6.022 x 10^{23} mol^{-1})

$[P.F]_{Y2Sn2O7}$ = 85% (in 180 min)

$= 0.85 \times 3.3 \times 10^{-5} \times 6.023 \times 10^{23}$

$= 16.89 \times 10^{18}$

$= 1.689 \times 10^{19}$

Therefore,

No. of Reacted electrons = $2 \times 1.689 \times 10^{19}$

$= 3.37 \times 10^{19}$

$$\text{Now, No. of Photons} = \frac{Light\ absorbed\ by\ the\ photocatalyst}{The\ average\ photon\ energy} \times t \qquad \text{..................... (8)}$$

Where; t= time taken for the reaction

Light Absorbed by the photocatalyst = H x A

H= Input from the Source of the Light=234 mW/cm^2 = 2340W/m^2

A= Illuminated Geometrical Surface Area of the Reactor Used = Illuminated Geometric irradiation area of the photocatalyst placed inside the photo-reactor = 0.00049 m^2 = 50% of the Geometric Surface area of the used reactor (Reference by Grätzel *et al.*[1])

Light absorbed by the photocatalyst= 2340 x 0.00049= 1.14 J/sec

The average photon energy = $\frac{hc}{\lambda}$

h =Planck's constant= 6.626×10^{-34} Jsec; c = velocity of light =3×10^{8} m/sec

λ = Maximum Emission Wavelength for the spectrum of the Source = 430 nm= 430×10^{-9} m

The average photon energy= 4.62×10^{-19}

Therefore,

No. of Photons = $1.14 / 4.62 \times 10^{-19} \times 240 \times 60$

= 3.53×10^{22} photons

AQE= $\frac{Number\ of\ reacted\ electrons}{Number\ of\ incident\ photons}$ x 100

= $3.3 \times 10^{19}/3.53 \times 10^{22} \times 100$

= 0. 093 %.

The above calculated Quantum Efficiency is the Apparent Quantum Efficiency= AQE of $Y_2Sn_2O_7$.

AQE of $Y_{0.4}Bi_{1.6}Sn_2O_7$

$[P.F]_{Y0.4Bi1.6Sn2O7}$ = 95.78% (in 150 min)

AQE= $\frac{Number\ of\ reacted\ electrons}{Number\ of\ incident\ photons}$ x 100 …………………………. (9)

As given in equation (1), during the photocatalytic p-CP oxidation, stoichimetrically 2, electrons are required to produce one molecule of CO_2. Though, this reaction is a multistep reaction as shown in the formation of the intermediates (and to be checked which is the slowest to determine the R.D.S.), however generically each step being a two electron step will mostly a two electron step.

$[P.F]_{Y0.4Bi1.6Sn2O7}$ = 95.78% (in 160 min)

= $0.9578 \times 3.3 \times 10^{-5} \times 6.023 \times 10^{23}$

= 19.03×10^{18}

= 1.903×10^{19}

No. of Reacted electrons = $2 \times 1.903 \times 10^{19}$

= 3.806×10^{19}

No. of Photons= $1.14 / 4.62 \times 10^{-19} \times 160 \times 60$

= 2368.83×10^{19} photons

$= 2.37 \times 10^{22}$ photons

AQE = $3.806 \times 10^{19}/2.37 \times 10^{22} \times 100$

$= 3.806/2.37 \times 10^{-1}$

$= 0.16\%$

AQE of $Y_{0.3}Bi_{1.7}Sn_2O_7$

[P.F] $Y_{0.3}Bi_{1.7}Sn_2O_7 = 98.68\%$ (in 150 min)

$$AQE = \frac{Number\ of\ reacted\ electrons}{Number\ of\ incident\ photons} \times 100 \qquad \ldots\ldots\ldots\ldots\ldots\ldots\ldots\ldots\ldots\ldots (10)$$

As given in equation (1), during the photocatalytic p-CP oxidation, stoichimetrically 2, electrons are required to produce one molecule of CO_2. Though this reaction is a multistep reaction as shown in the formation of the intermediates (and to be checked which is the slowest to determine the R.D step), however generically each step being a two electron step will mostly a two electron step.

[P.F] $_{Y0.3Bi1.7Sn2O7} = 98.68\%$ (in 140 min)

$= 0.9868 \times 3.3 \times 10^{-5} \times 6.023 \times 10^{23}$

$= 19.62 \times 10^{18}$

$= 1.962 \times 10^{19}$

No. of Reacted electrons $= 2 \times 1.962 \times 10^{19}$

$= 3.924 \times 10^{19}$

No. of Photons $= 1.14 / 4.62 \times 10^{-19} \times 140 \times 60$

$= 2072.73 \times 10^{19}$ photons

$= 2.073 \times 10^{22}$ photons

AQE = $3.924 \times 10^{19}/2.073 \times 10^{22} \times 100$

$= 3.924/2.073 \times 10^{-1}$

$= 0.19\%$

AQE of $Y_{0.1}Bi_{1.9}Sn_2O_7$

[P.F] $_{Y0.1Bi1.9Sn2O7} = 100\ \%$ (in 90 min)

$$AQE = \frac{Number\ of\ reacted\ electrons}{Number\ of\ incident\ photons} \times 100 \qquad \ldots\ldots\ldots\ldots\ldots\ldots\ldots\ldots\ldots\ldots (11)$$

As given in equation (1), during the photocatalytic p-CP oxidation, stoichimetrically 2, electrons are required to produce one molecule of CO_2. Though, this reaction is a multistep reaction as shown in the formation of the intermediates (and to be checked which is the slowest to determine the R.D.S.), however generically each step being a 2 electron step will mostly a two electron step.

$[P.F]_{Y0.1Bi1.9Sn2O7} =$ 98.68% (in 90 min)

$= 1.0 X 3.3 X 10^{-5} X 6.023 X 10^{23}$

$= 19.87 x 10^{18}$

$= 1.987 x 10^{19}$

No. of Reacted electrons = $2 x 1.987 x 10^{19}$

$= 3.975 x10^{19}$

No. of Photons = $1.14 / 4.62 x 10^{-19} x 100 x 60$

$= 1480.52 x 10^{19}$ photons

$= 1.481X 10^{22}$ photons

AQE= $3.924x 10^{19}/1.481x10^{22} x100$

$= 3.806/2.37 x 10^{-1}$

=0.26%

AQE of $Bi_2Sn_2O_7$

100 % [P.F] (in 60 min)

$$AQE= \frac{Number\ of\ reacted\ electrons}{Number\ of\ incident\ photons} x 100 \qquad \ldots\ldots\ldots\ldots\ldots\ldots\ldots\ldots\ldots\ldots (12)$$

As given in equation (1), during the photocatalytic p-CP oxidation, stoichimetrically 2, electrons are required to produce one molecule of CO_2. Though, this reaction is a multistep reaction as shown in the formation of the intermediates (and to be checked which is the slowest to determine the R.D step), however generically each step being a 2 electron step will mostly a two electron step.

$[P.F]_{Bi2Sn2O7} = 100$ % in 60 min

$=1.0 X 3.3 X 10^{-5} X 6.023 X 10^{23}$

$= 19.879 x 10^{18}$

$= 1.9879 x 10^{19}$

Therefore,

No. of Reacted electrons = $2 x 1.9879 x 10^{19}$

$= 3.97 x10^{19}$

No. of Photons = 1.14 / 4.62 x 10^{-19} x 60x60

= 0.88 x 10^{22} photons

A.Q.E = 3.97 x10^{19}/0.88 x 10^{22} x 100

= 3.97/0.88 X10^{-1}

=0.456 %

Catalysts	**AQE (%)**
$Y_2Sn_2O_7$	0. 093
$Y_{0.4}Bi_{1.6}Sn_2O_7$	0.16
$Y_{0.3}Bi_{1.7}Sn_2O_7$	0.19
$Y_{0.1}Bi_{1.9}Sn_2O_7$	0.26
$Bi_2Sn_2O_7$	0.456

Table S-2: Calculated Apparent Quantum efficiencies of different photocatalysts.

8. DR-UV-Vis spectra for photocatalysts

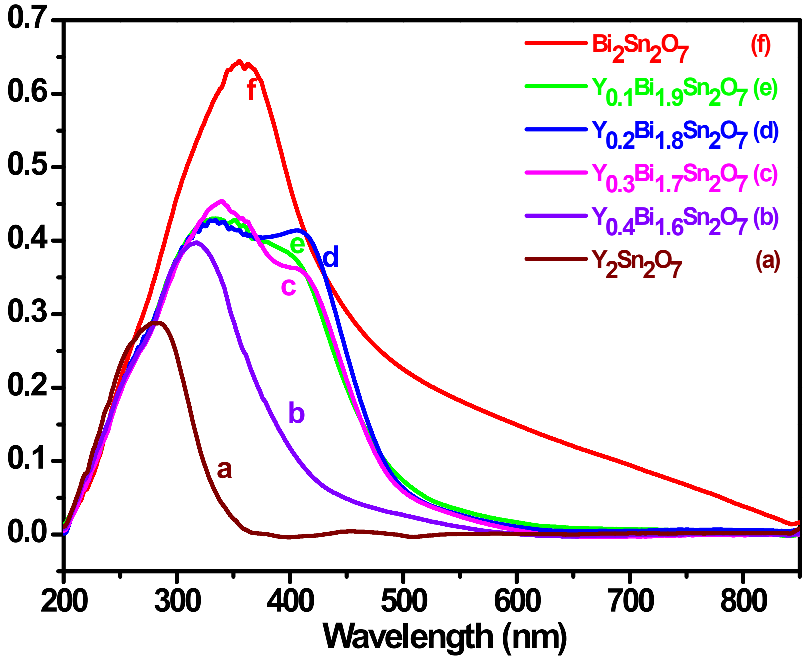

Fig.S-17: DR-UV-Vis Spectra for the $Y_{2-x}Bi_xSn_2O_7$ samples where a) $Y_2Sn_2O_7$; b) $Y_{0.4}Bi_{1.6}Sn_2O_7$; c) $Y_{0.3}Bi_{1.7}Sn_2O_7$; d) $Y_{0.2}Bi_{1.8}Sn_2O_7$; e) $Y_{0.1}Bi_{1.9}Sn_2O_7$; f) $Bi_2Sn_2O_7$.

9. Comparison of UV irradiation of photocatalysts.

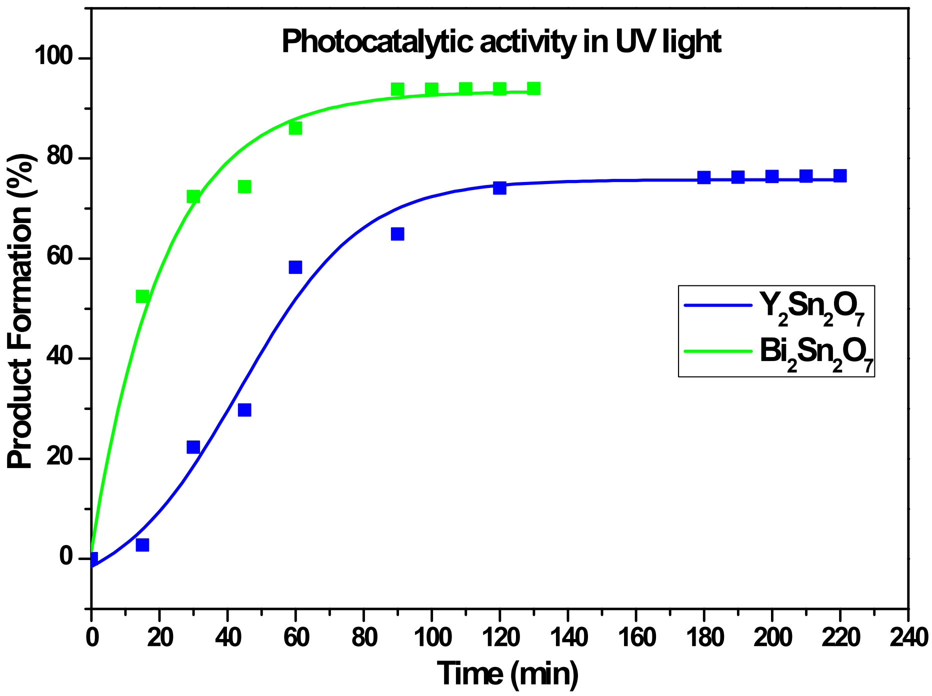

Fig. S-18: Comparison the $Y_2Sn_2O_7$ and the $Bi_2Sn_2O_7$ photocatalysts with the UV -irradiation for degradation of p-CP of the same concentration.

10. FTAS details of BSN photocatalysts

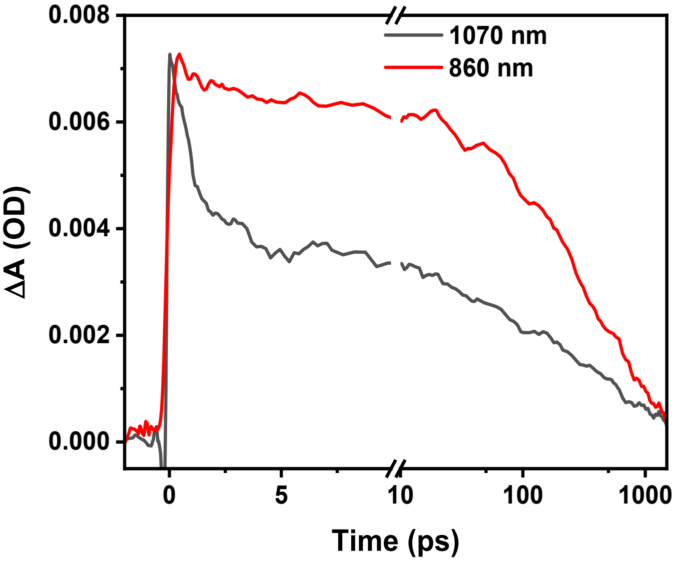

Figure S-19: Transient decay kinetics recorded at 860 nm and 1070 nm for water dispersed BSN solution

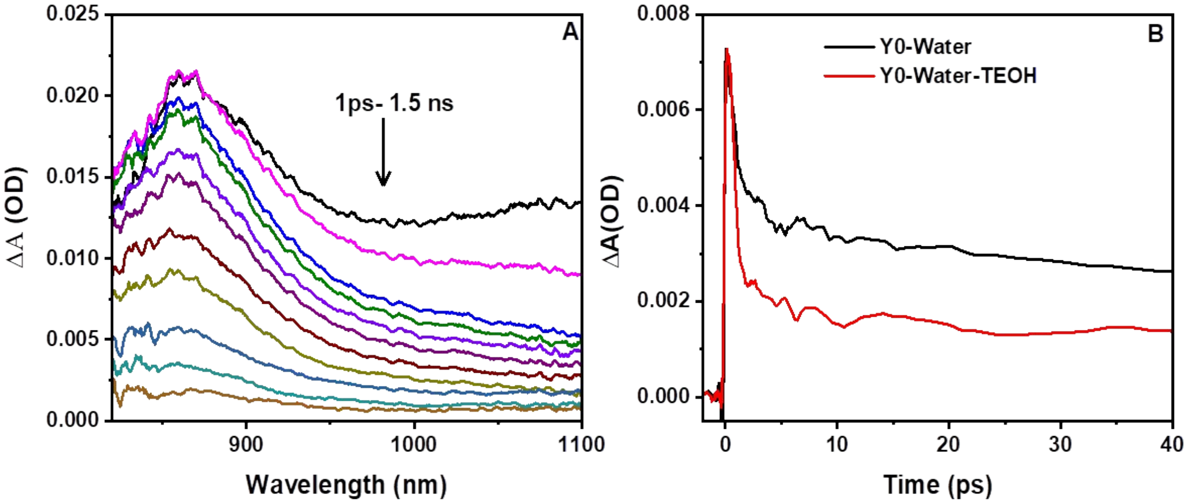

Fig. S-20: (A) Transient absorption spectra of water dispersed $Bi_2Sn_2O_7$ in presence of 2 M triethanolamine (TEA) at different delay times. (B) The decay kinetics of the transient at 1070 nm for water dispersed solution of $Bi_2Sn_2O_7$ in absence and presence of 2 M TEA.

11. Complete Mineralization of p-CP with different photocatalysts and Mass spectroscopic evaluation

Complete mineralization experiments in closed photocatalytic reactor and detection by Mass Spectroscopy.

Photocatalytic mineralization experiments were carried out using a closed quartz photocatalytic reactor (volume-90 ml) (Fig. S-X) attached with a glass valve for evacuation using 60 ml of *p-CP* solution with a molar concentration of 3.3×10^{-5} mol/dm^3 (pH~ 6) and 100 mg of the photocatalytic materials. The photocatalytic reactions were monitored using a quadruple based mass spectroscopic instrument Extorr RGA having a mass range of (1-200) under 10^{-7} mbar pressure with a sample pressure of 10^{-6}. Prior to taking the experimental data initially the mass spectra of air were taken and a calibration curve for the CO_2 in air mixture was obtained. The CO_2 air mixture for the calibration curve was carried out by making a CO_2 air simulative mixture in an evacuated glass bulb. Three different calibration curve (in different concentration regime) for the CO_2 concentration in mass spectrometer was fitted with a linear fit in ORIGIN software with (Adj R^2 ~ 0.998).

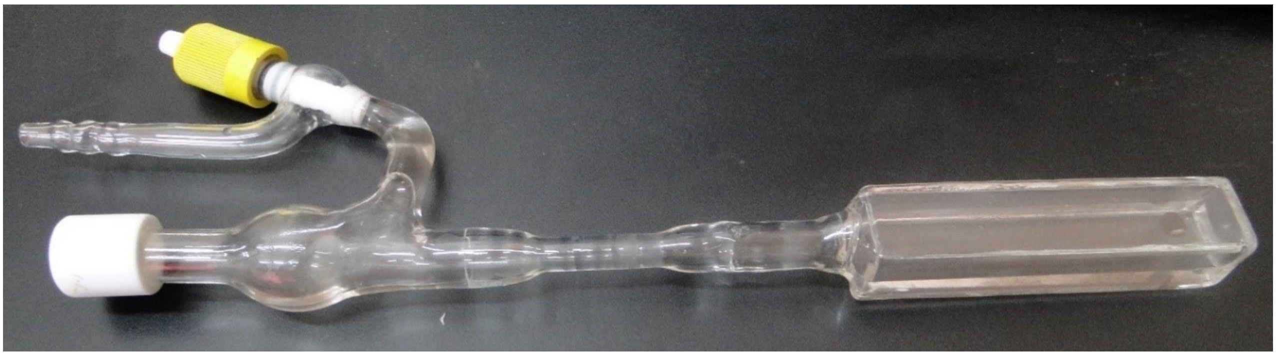

Fig. S-21-A- The experiments have been conducted in the above photocatalytic reactor.

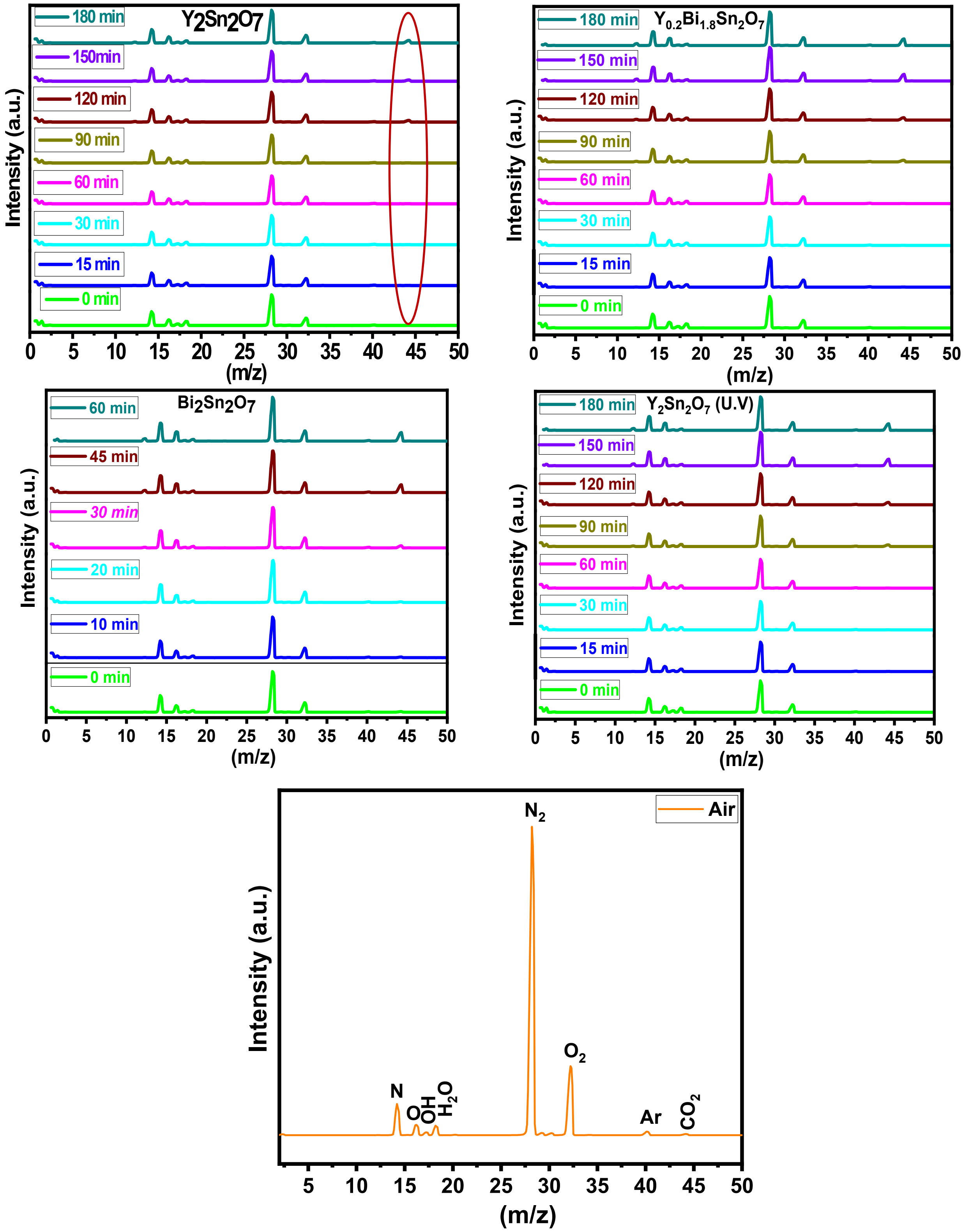

Fig. S-21-B: The complete-oxidation of p-CP with a closed photocatalytic reactor under visible irradiation and the product being studied in the mass spectroscopy; 1) $Y_2Sn_2O_7$; 2) $Y_{0.2}Bi_{1.8}Sn_2O_7$; 3) $Bi_2Sn_2O_7$; p-CP mineralization under UV radiation for $Y_2Sn_2O_7$.

Volume of CO_2 formed analysed from the calibration curve from the mass spectroscopic data =A

Amount of CO_2 to be formed stoichimetrically from the volume of p-CP present where it is completely oxidised to CO_2 = B

Percentage of product Formed (CO_2 %) = $\frac{A}{B}$ x 100 ………. (13)

12. TG-Studies

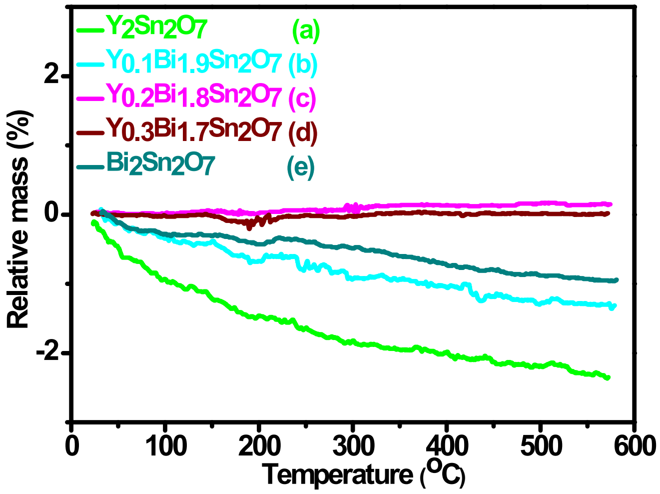

Fig.S.22: TGA study of the different set of catalysts (a) $Y_2Sn_2O_7$, (b) $Y_{0.1}Bi_{1.9}Sn_2O_7$, (c) $Y_{0.2}Bi_{1.8}Sn_2O_7$, (d) $Y_{0.3}Bi_{1.7}Sn_2O_7$ and (e) $Bi_2Sn_2O_7$.

13. ^{119}Sn- NMR

Nuclear magnetic resonance (NMR) spectroscopy offers a valuable tool for probing the local structure of nuclei that are NMR-active. Figure 8 depicts the ^{119}Sn magic angle spinning (MAS) solid-state NMR (SSNMR) spectra of six distinct samples, acquired at a MAS frequency of 4 kHz. These spectra provide insights into the impact of Bi doping on the local environment surrounding Sn. The observed line shape corresponds to a powder pattern, which arises from the phenomenon of chemical shift anisotropy (CSA). CSA stems from the orientation dependence of the chemical shift experienced by a nucleus within a molecule. Analysis of the spinning CSA sideband pattern allows for the extraction of information regarding the electron density distribution surrounding the nucleus, its molecular motion, and the molecule's orientation relative to the local magnetic field. The spectrum of the unsubstituted $Y_2Sn_2O_7$ bulk sample exhibits a sharp peak with a chemical shift value of approximately -581 ppm (Figure 8.f). This excellent agreement with previously reported spectra for the $Y_2Sn_2O_7$ phase with an ordered pyrochlore structure .[54 ,55] This strongly suggests the presence of an ordered pyrochlore structure in the unsubstituted sample. Furthermore, the chemical shift value of -581 ppm corroborates the octahedral coordination environment surrounding Sn^{4+} ions, with 6 oxygen atoms as nearest neighbours and 12 next-nearest neighbours (NNN) consisting of six Y^{3+} and six Sn^{4+} ions.

In contrast, $Bi_2Sn_2O_7$ possesses a significantly more complex structure, featuring SnO_6 octahedra surrounded by distorted trigonal bipyramidal Bi polyhedra (BiO_5). This stark difference in the local environment surrounding Sn between $Y_2Sn_2O_7$ and $Bi_2Sn_2O_7$ translates to a distinct resonance chemical shift value of 598 ppm for ^{119}Sn in $Bi_2Sn_2O_7$ (Fig. 8.a). Interestingly, the Bi-substituted samples exhibit a constant anisotropy parameter value, implying minimal alterations to the local environment surrounding the ^{119}Sn nucleus despite increasing Bi doping concentration. The CSA tensor in the principal axis system (PAS) is characterized **by** its principal components (δ_{11}, δ_{22}, and δ_{33}). These components are used to describe the observed powder pattern through the following expression: $\delta(\alpha, \beta) = \delta_{11} \sin^2 \beta \cos^2 \alpha + \delta_{22} \sin^2 \beta \sin^2 \alpha + \delta_{33} \cos^2 \beta$, where α and β represent the Euler angles [56]. The CSA parameters are determined using the DMFIT software [57]. Table 5 summarizes the isotropic chemical shift (δ_{iso}), anisotropy parameter, and asymmetry parameter for $Y_{1-x}Bi_xSn_2O_7$ (x = 0.4 to 1.6). The spectra of $Y_{0.1}Bi_{1.9}Sn_2O_7$, $Y_{0.2}Bi_{1.8}Sn_2O_7$, $Y_{0.3}Bi_{1.7}Sn_2O_7$, $Y_{0.4}Bi_{1.6}Sn_2O_7$ exhibit an asymmetry parameter value of zero, indicating an axially symmetric electronic distribution around the ^{119}Sn nucleus (Fig. 8). This observation signifies a minimal perturbation to the electronic environment surrounding Sn upon partial Y substitution with Bi. In stark contrast, the ^{119}Sn MAS SSNMR spectrum of $Y_2Sn_2O_7$ (Fig. 8.f) deviates significantly from the spectra of the other five compounds. This marked difference suggests a drastic alteration in the local environment surrounding the ^{119}Sn nucleus when Y is partially substituted by Bi. The ^{119}Sn MASSSNMR spectrum of $Bi_2Sn_2O_7$ (Fig. 8.a) exhibits a dramatic transformation and cannot be adequately modelled using conventional approaches. This observation underscores a substantial change in the electronic environment surrounding the ^{119}Sn nucleus upon Yttrium replacement with Bismuth.

Name of the compound	$\delta_{iso} = \frac{\delta_{11} + \delta_{22} + \delta_{33}}{3}$ (ppm)	$Anisotropy \equiv \Delta\delta = \delta_{33} - \frac{(\delta_{11} + \delta_{22})}{2}$ **(ppm)**	$Asymmetry \equiv \eta = \frac{(}{(}$
$(Y_{2-x}Bi_xSn_2O_7)$ $(x\cong1.6)$	-600.1	-90.4	0.0
$(Y_{2-x}Bi_xSn_2O_7)$ $(x\cong1.7)$	-600.2	-85.0	0.0
$(Y_{2-x}Bi_xSn_2O_7)$ $(x\cong1.8)$	-600.1	-90.4	0.0
$(Y_{2-x}Bi_xSn_2O_7)$ $(x\cong1.9)$	-601.0	-78.0	0.0

Table S-3 : Chemical shift anisotropy (CSA) parameter

{Note: The magnitude of the anisotropy parameter $\Delta\delta = \delta_{33} - (\delta_{11} + \delta_{22})/2$ determines the largest distance of separation of the spinning CSA sideband pattern from the centre of gravity $(\delta_{iso} = (\delta_{11} + \delta_{22} + \delta_{33})/3)$, and the sign of the anisotropy parameter indicates the side of the center of gravity where the separation distance is maximal. Asymmetry parameter $\eta = (\delta_{22} - \delta_{11})/(\delta_{33} - \delta_{iso})$ measures how much the spinning CSA sideband pattern is deviated from its axially symmetric value.

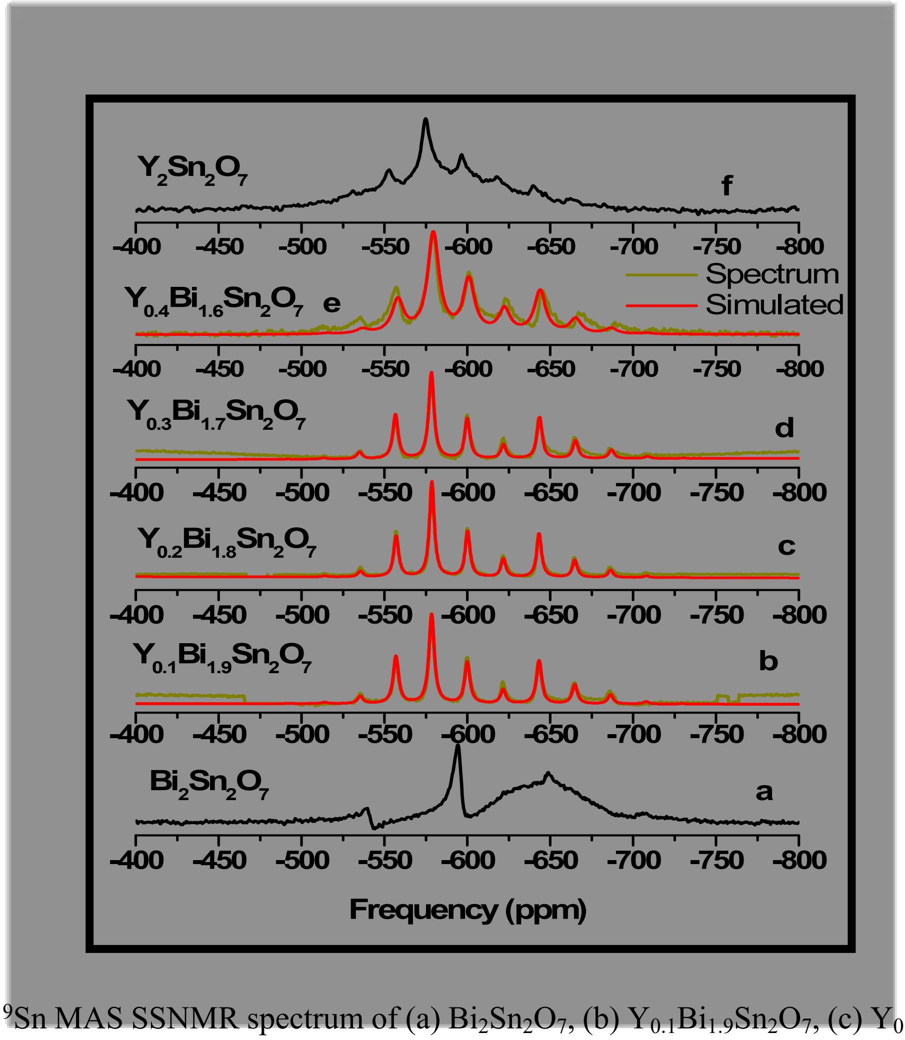

Fig.S. 23: ^{119}Sn MAS SSNMR spectrum of (a) $Bi_2Sn_2O_7$, (b) $Y_{0.1}Bi_{1.9}Sn_2O_7$, (c) $Y_{0.2}Bi_{1.8}Sn_2O_7$, (d) $Y_{0.3}Bi_{1.7}Sn_2O_7$, (e) $Y_{0.4}Bi_{1.6}Sn_2O_7$, and (f) $Y_2Sn_2O_7$ at magic angle spinning (MAS) at frequency 4 kHz.

14. Effect of pH, H_2O_2, hole quencher and radicals quencher over photocatalytic activity.

In the photo-degradation reaction, 100 mg of BSN photocatalyst sample was introduced into a 60 ml p-CP solution with a molar concentration of 3.3×10^{-5} mol/dm^3. For the hole quenching experiment triethanol ammine (TEA) (with concentration – 0.112M) has been added in the p-CP water mixture before being irradiated with the visible irradiation. In order to check the effect of the H_2O_2 (or ·OOH-radical) on reaction kinetics, 0.1 cc of H_2O_2 mixture (29-32 w/w %) was added with the 60 ml p-CP solution. Similar experiments were conducted with the 100 mg YSN catalyst with the UV irradiator with similar experimental conditions. **Effect of pH- Acidic pH**

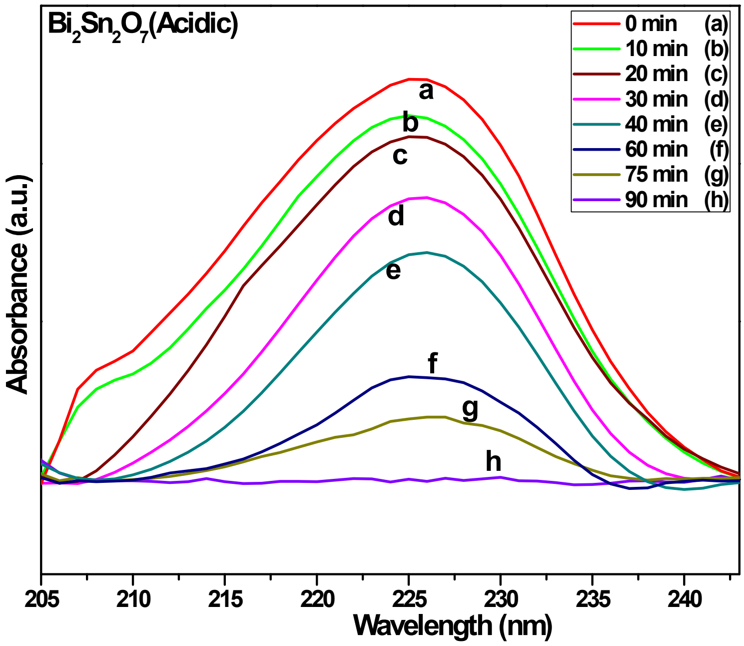

Fig.S.24. Degradation of p-CP in acidic condition (pH-4) using $Bi_2Sn_2O_7$ photocatalyst as a function of time.

The effect of pH was understood at pH -4 (the pH was regulated using 10^{-4}N HCl in the p-CP solution and the pH was finally measured using a pH meter) and pH-10 (where the pH was controlled using a 10^{-4} N NaOH in the p-CP solution and finally the pH of the solution was checked using a pH meter). Subsequently, these systems were exposed to visible light, and at every 10 min interval, one system was withdrawn for absorbance measurement using a UV-Vis spectrophotometer. Post each measurement, the mixtures underwent an additional 10 minutes of stirring. The optical absorption measurement of the supernatant was carried out on a JASCO UV-670 spectrophotometer at the wavelength $\lambda = 225$ nm, corresponding to the absorption spectrum's maximum for the p-CP solution. The evaluation of photocatalytic activity was performed thrice to ensure result repeatability. The results for the effect of pH, H_2O_2 and TEA (hole quencher) is given below. The plot shown below are given after the base line correction and therefore are quantitative in nature.

A) **Basic pH**

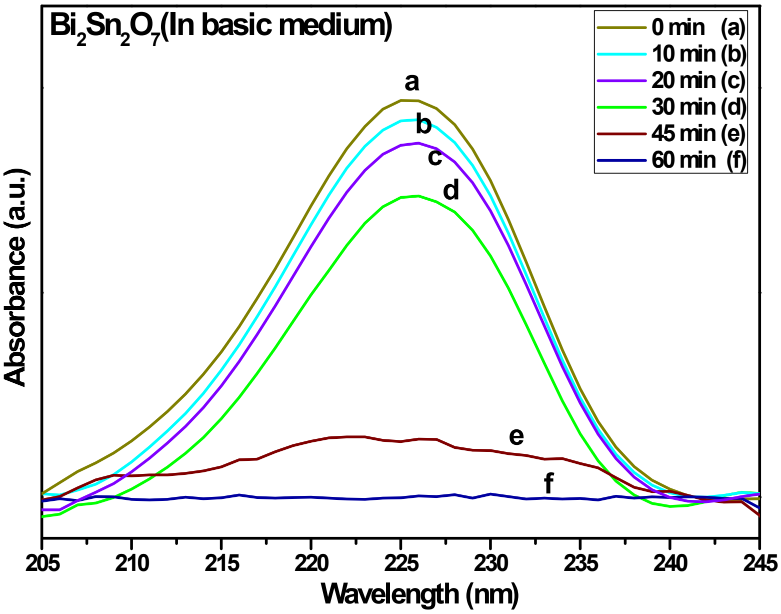

Fig.S.25. Degradation of p-CP in basic condition (pH-10) using $Bi_2Sn_2O_7$ photocatalyst as a function of time.

B) **Effect of H_2O_2 (·OOH -radical)**

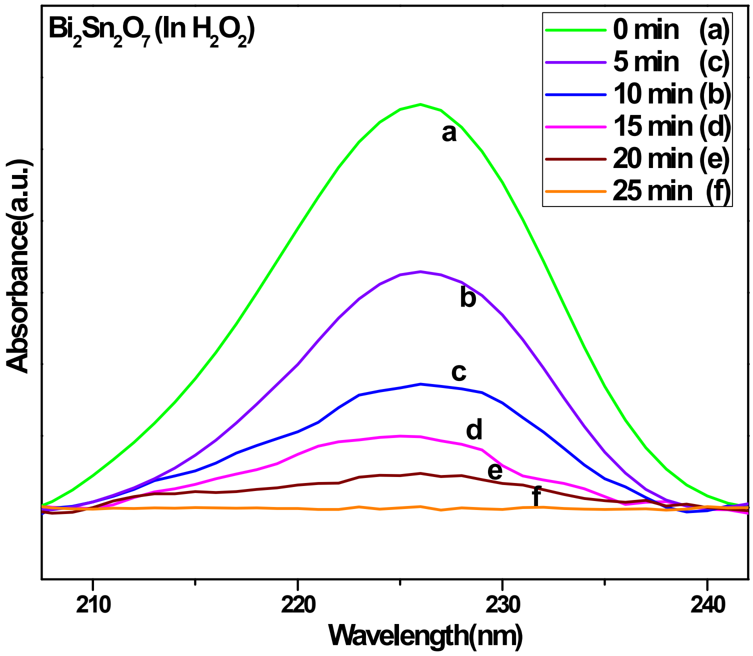

Fig.S.26-A. Degradation of p-CP in presence of H_2O_2 using $Bi_2Sn_2O_7$ photocatalyst as a function of time.

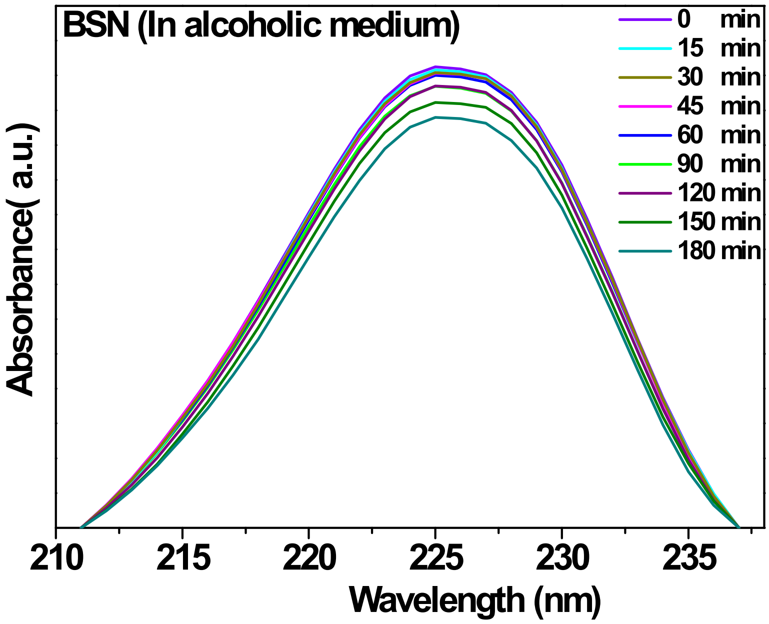

Fig.S.26-B. Degradation of p-CP in presence of isopropanol using $Bi_2Sn_2O_7$ photocatalyst as a function of time.

Quenching refers to a process where the excited state of a molecule is deactivated or its fluorescence is suppressed, often through energy transfer or reaction with another molecule. Mostly certain quenchers are used as radical scavengers in order to prove the effective role of a particular H. or

OH. radical in the photocatalytic processes. The alcohols are generically treated as universal quencher to scavenge both H• as well as OH• . In the case of H and OH radicals, the quenching process involves their reaction with the alcohol (R-OH) molecule. A common reaction is hydrogen abstraction, where the H radical removes a hydrogen atom from the alcohol molecule (R-OH) to form a stable molecule and a new radical. For example: H• + R-OH → H_2 + R-O• .[34] The OH radical can react with the alcohol molecule in various ways, including hydrogen abstraction, but it can also form an adduct (H_2O-R), which can further react or decompose. This reaction is a type of radical addition, where the OH radical adds to the alcohol, and then undergoes a proton transfer to form the alkyl radical and water and the efficiency of alcohol quenching can depend on factors such as the structure of the alcohol (e.g., primary, secondary, tertiary) and the concentration of the radical being quenched. Tertiary alcohols tend to be more reactive in these reactions due to the stability of the resulting radical. [35, 36, 37, 38]. Therefore, to show the effect of radical intermediates (·OH, ·H) conclusively for the p-CP degradation isopropanol was used as a universal quencher for both H• as well as OH•. 5ml of 0.1 M IPA was added and under the similar condition using $Bi_2Sn_2O_7$ (BSN). The Fig .1 shows that the BSN is slowed down very substantially after using the isopropanol as a H• as well as OH• quencher and even after 180 minutes the p-CP is not degraded more than 20%. Whereas, without isopropanol the-CP is mineralized to CO_2 by BSN in 60 min. This clearly shows the direct involvement of H• or and OH•.

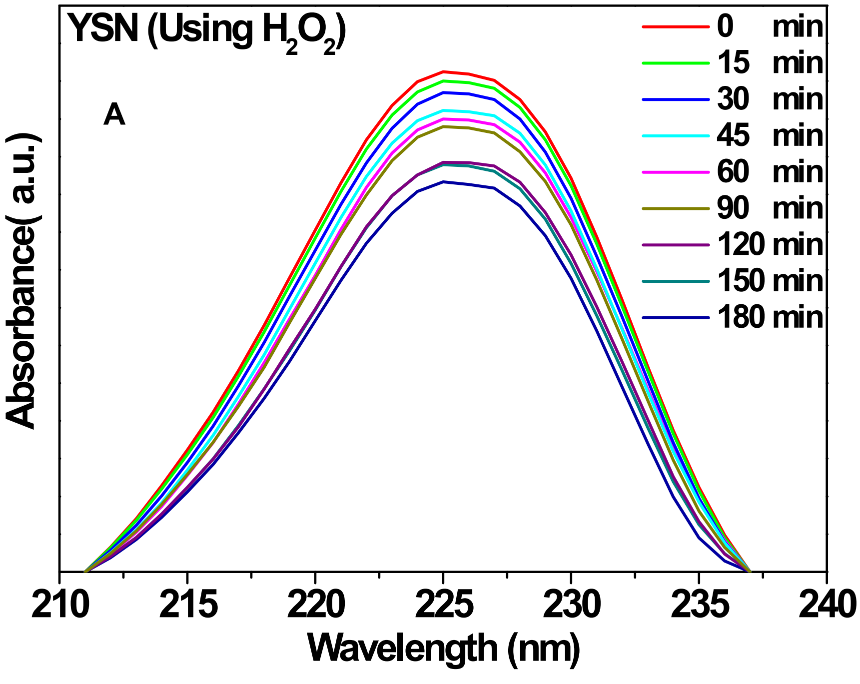

Fig.S.26-C. Degradation of p-CP in presence of H_2O_2 using $Y_2Sn_2O_7$ photocatalyst as a function of time.

We have performed another control experiment to understand the effect of UV-irradiation over the YSN and the BSN photocatalysts. It was earlier quite clear that the photocatalytic reaction the kinetics for the mineralization becomes quite faster if H_2O_2 is added to the reaction conditions under visible conditions using BSN photocatalyst (Fig.4.B). Similarly however, under UV conditions with the YSN photocatalyst the photocatalytic reaction becomes slower as has been shown in the Fig.4.A. Around, 0.1 cc of H_2O_2 mixture (29-32 w/w %) was added with the 60 ml p-CP solution in order to check the effect of the H_2O_2 (or •OOH-radical) on reaction kinetics with 100 mg of YSN photocatalyst. However, in this case the reaction rate was very slow showing the fact that the H_2O_2 (OOH• radical) does not facilitate the UV photoreaction. As these photocatalysts performs p-CP mineralization via hole mediated reaction indirectly, so the major component that affects the reaction rates will be the H• and the OH• radicals. The OH• radicals under UV condition mostly forms H_2O_2 which affects the BSN reaction positively and the YSN reaction negatively making the BSN photocatalyst a better one as compared to YSN under UV conditions.

C) **Effect of TEA (Triethanol Ammine-hole quencher)**

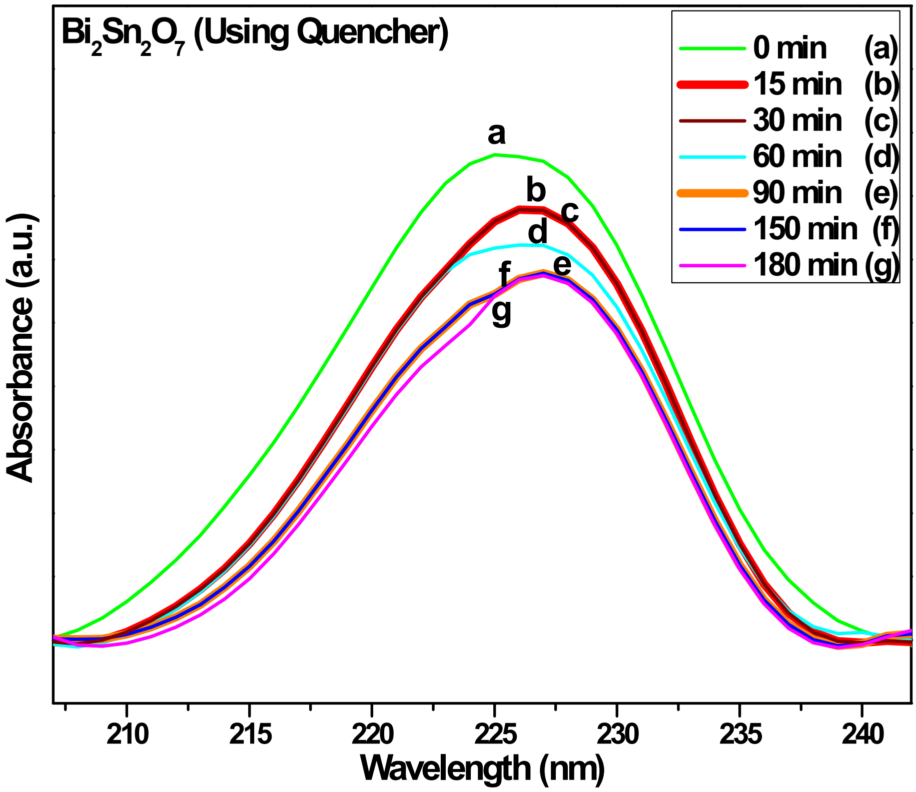

Fig.S.27. Degradation of p-CP in presence of hole quencher (triethyl amine) using $Bi_2Sn_2O_7$ photocatalyst as a function of time.

Consequently, the percentage of degradation products is calculated using Equation-1 (as provided in the main text).

The product percentage (P.C %) is

P.C (%) = [(Co-Ci) /Co] x 100 ………………….. (1)

Where,

Co = UV-Vis Intensity of the p-CP without any catalyst

Ci= UV-Vis Intensity of p-CP without particular photocatalyst at time t_i.

In order to have a quantitative understanding, catalytic performance activity for the different photocatalysts was plotted against time and is presented in Fig.9.D. The generic explanation is provided in the main text.

15. XRD and Elemental calculation from XPS of photocatalysts after catalytic activity

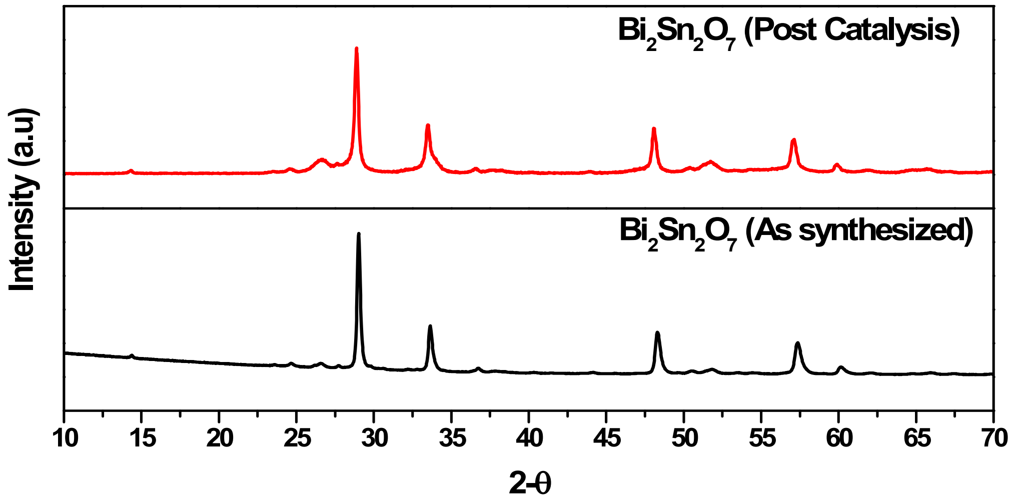

Fig. S.28-A. XRD of $Bi_2Sn_2O_7$ a) As synthesised and b) Post Catalytic Treatment.

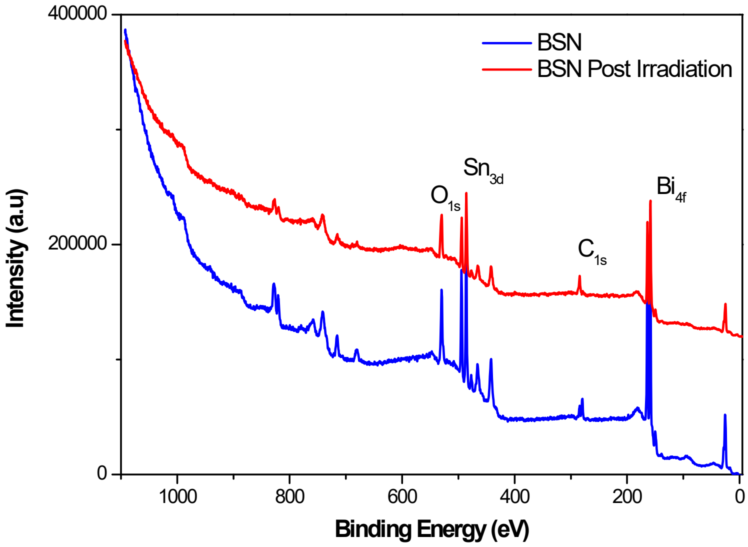

Fig.S-28-B: Survey Scans of the BSN as synthesized and BSN after photocatalytic irradiation.

BSN-Before Photocatalysis				**BSN-After Photocatalysis**			
Element	Position	FWHM	Atom (%)	Element	Position	FWHM	Atom (%)
Bi-4f	158.2	2.0	16.8	Bi-4f	158.2	2.0	16.2
Sn-3d	480.2	2.0	14.3	Sn-3d	480.2	2.0	18.7
O-1s	530.7	3.5	68.9	O-1s	530.7	3.5	65.1

Table -S-4: Elemental composition of BSN photocatalyst from XPS before and after photo-irradiation.

References

1 . Poswal, A. K.; Agrawal, A.; Yadav, A. K.; Nayak, C.; Basu, S.; Kane, S. R.; Garg, C. K.; Bhattachryya, D.; Jha, S. N.; Sahoo, N. K. Commissioning and First Results of Scanning Type EXAFS Beamline (BL-09) at INDUS-2 Synchrotron Source. *AIP Conf. Proc*. 2014, **1591**(1), 649–651.

2 . Basu, S.; Nayak, C.; Yadav, A. K.; Agrawal, A.; Poswal, A. K.; Bhattacharyya, D.; Jha, S. N.; Sahoo, N. K. A Comprehensive Facility for EXAFS Measurements at the INDUS-2 Synchrotron Source at RRCAT, Indore, India. *J. Phys. Conf. Ser.* 2014, **493**(1), 012032.

3 . Koningsberger, D. C.; Prins, R. X-Ray Absorption: Principles, Applications, Techniques of EXAFS, SEXAFS and XANES; *John Wiley and Sons Inc*., New York, NY, USA, 1987.

4 . Ravel, B.; Newville, M. ATHENA, ARTEMIS, HEPHAESTUS: Data Analysis for X-Ray Absorption Spectroscopy Using IFEFFIT. *J. Synchrotron Radiat*. 2005, **12**, 537–541.

5 . Gu, Y.; Jiang, X.; Sun, W.; Bai, S.; Dai, Q.; Wang, X. 1,2-Dichloroethane Deep Oxidation over Bifunctional Ru/CexAly Catalysts. *ACS Omega* 2018, **3**(8), 8460–8470.

6 . Han, A.; Zhang, H.; Lu, D.; Sun, J.; Chuah, G. K.; Jaenicke, S. Efficient Photodegradation of Chlorophenols by BiOBr/NaBiO3 Heterojunctioned Composites under Visible Light. *J. Hazard. Mater.* 2018, **341**, 83–92.

7 . Walsh, A.; Watson, G. W.; Payne, D. J.; Atkinson, G.; Egdell, R. G. A Theoretical and Experimental Study of the Distorted Pyrochlore Bi2Sn2O7. *J. Mater. Chem*. 2006, **16**(34), 3452–3458.

8 . Chen, M.; Tanner, D. B.; Nino, J. C. Infrared Study of the Phonon Modes in Bismuth Pyrochlores. *Phys. Rev. B* 2005, **72**(5), 054303.

9 . Li, D.; Xue, J. Synthesis of Bi2Sn2O7 and Enhanced Photocatalytic Activity of Bi2Sn2O7 Hybridized with C3N4. *New J. Chem*. 2015, **39**(7), 5833–5840.

10 . Tian, J.; Peng, H.; Xu, X.; Liu, W.; Ma, Y.; Wang, X.; Yang, X. High Surface Area La2Sn2O7 Pyrochlore as a Novel, Active and Stable Support for Pd for CO Oxidation. *Catal. Sci.* Technol. 2015, **5**(4), 2270–2281.

11 . Zhang, T.; Li, K.; Zeng, J.; Wang, Y.; Song, X.; Wang, H. Synthesis and Structural Characterization of a Series of Lanthanide Stannate Pyrochlores. *J. Phys. Chem. Solids* 2008, **69**, 2845–2851.

12 . Johnson, S. K.; Houk, L. L.; Feng, J. R.; Houk, R. S.; Johnson, D. C. Electrochemical Incineration of 4-Chlorophenol and the Identification of Products and Intermediates by Mass Spectrometry. *Environ. Sci. Technol*. 1999, **33**(15), 2638–2644.

13 . Evans, I. R.; Howard, J. A. K.; Evans, J. S. O. α-Bi2Sn2O7 – a 176 Atom Crystal Structure from Powder Diffraction Data. *J. Mater. Chem*. 2003, **13**(9), 2098–2103.

14 . Shalygin, A.; Malysheva, L.; Paukshtis, E. Mechanism of 1,2-Dichloroethane Dehydrochlorination on the Acid Sites of Oxide Catalysts as Studied by IR Spectroscopy. *Kinet. Catal*. 2011, **52**, 236–243.

15 . Mandal, B.; Krishna, P.; Tyagi, A. K. Order–Disorder Transition in the Nd2−yYyZr2O7 System: Probed by X-Ray Diffraction and Raman Spectroscopy. *J. Solid State Chem*. 2010, **183**, 41–45.

16 . Feng, X.; Xu, J.; Xu, X.; Zhang, S.; Ma, J.; Fang, X.; Wang, X. Unraveling the Principles of Lattice Disorder Degree of Bi2B2O7 (B = Sn, Ti, Zr) Compounds on Activating Gas Phase O2 for Soot Combustion. *ACS Catal*. 2021, **11**(19), 12112–12122.

17 . Kirikova, N. Yu.; Krupa, J. C.; Makhov, V. N.; Severac, C. XPS Studies of the Energy Band Structure of Three Y3+-Based Fluoride Compounds. J. Electron *Spectrosc. Relat. Phenom*. 2002, **122**(1), 85–89.

18 . Long, M.; Ilhan, Z. E.; Xia, S.; Zhou, C.; Rittmann, B. E. Complete Dechlorination and Mineralization of Pentachlorophenol (p-CP) in a Hydrogen-Based Membrane Biofilm Reactor (MBfR). *Water Res*. 2018, **144**, 134–144.

19 . He, M.; Li, W.; Jiexiang, X.; Xu, L.; Di, J.; Hui, X.; Yin, S.; Li, H.; Li, M. The Enhanced Visible Light Photocatalytic Activity of Yttrium-Substituted BiOBr Synthesized via a Reactable Ionic Liquid. *Appl. Surf. Sci*. 2015, **331**, 135–143.

20 . Humayun, M.; Hu, Z.; Khan, A.; Cheng, W.; Yuan, Y.; Zheng, Z.; Fu, Q.; Luo, W. Highly Efficient Degradation of 2,4-Dichlorophenol over CeO2/g-C3N4 Composites under Visible-Light Irradiation: Detailed Reaction Pathway and Mechanism. *J. Hazard. Mater*. 2019, *364*, 635–644.

21 . Czaplicka, M.; Kaczmarczyk, B. Infrared Study of Chlorophenols and Products of Their Photodegradation. *Colloq. Spectrosc. Int.* XXXIV 2006, **70**(5), 940–949.

22 . Zhu, C.; Wei, X.; Li, W.; Pu, Y.; Sun, J.; Tang, K.; Wan, H.; Ge, C.; Zou, W.; Dong, L. Crystal-Plane Effects of CeO2{110} and CeO2{100} on Photocatalytic CO2 Reduction: Synergistic Interactions of Oxygen Defects and Hydroxyl Groups. *ACS Sustain. Chem. Eng*. 2020, **8**(38), 14397–14406.

23 . Albonetti, S.; Blasioli, S.; Bonelli, R.; Mengou, J. E.; Scirè, S.; Trifirò, F. The Role of Acidity in the Decomposition of 1,2-Dichlorobenzene over TiO2-Based V2O5/WO3 Catalysts. *Appl. Catal. Gen*. 2008, **341**(1), 18–25.

24 . Yang, C. C.; Chang, S. H.; Hong, B. Z.; Chi, K. H.; Chang, M. B. Innovative PCDD/F-Containing Gas Stream Generating System Applied in Catalytic Decomposition of Gaseous Dioxins over V2O5–WO3/TiO2-Based Catalysts. *Chemosphere* 2008, **73**(6), 890–895.

25 . van den Brink, R. W.; Krzan, M.; Feijen-Jeurissen, M. M. R.; Louw, R.; Mulder, P. The Role of the Support and Dispersion in the Catalytic Combustion of Chlorobenzene on Noble Metal Based Catalysts. *Appl. Catal. B Environ*. 2000, **24**(3), 255–264.

26 . Liu, Y.; Wei, Z.; Feng, Z.; Luo, M.; Ying, P.; Li, C. Oxidative Destruction of Chlorobenzene and O-Dichlorobenzene on a Highly Active Catalyst: MnOx/TiO2–Al2O3. *J. Catal.* 2001, **202**(1), 200–204.

27 . Du, C.; Lu, S.; Wang, Q.; Buekens, A. G.; Ni, M.; Debecker, D. P. A Review on Catalytic Oxidation of Chloroaromatics from Flue Gas. *Chem. Eng. J.* 2018, **334**, 519–544.

28 . Nishiyama, N.; Fujiwara, Y.; Adachi, K.; Inumaru, K.; Yamazaki, S. Preparation of porous metal-ion-substituted titanium dioxide and the photocatalytic degradation of 4-chlorophenol under visible light irradiation. *Appl. Catal. B: Environ*. 2015, **176**, 347–353.

29 . Chai, Y.; Ding, J.; Wang, L.; Liu, Q.; Ren, J.; Dai, W.-L. Enormous enhancement in photocatalytic performance of Ag3PO4/HAp composite: A Z-scheme mechanism insight. *Appl. Catal. B: Environ.* 2015, **179**, 29–36.

30 . Lin, X.; Guo, X.; Shi, W.; Zhao, L.; Yan, Y.; Wang, Q. Ternary heterostructured Ag–BiVO4/InVO4 composites: Synthesis and enhanced visible-light-driven photocatalytic activity. *J. Alloys Compd*. 2015, **635**, 256–264.

31 . Aguilar, C. A. H.; Pandiyan, T.; Arenas-Alatorre, J. A.; Singh, N. Oxidation of phenols by TiO2Fe3O4M (M= Ag or Au) hybrid composites under visible light. *Sep. Purif. Technol*. 2015, **149**, 265–278.

32 . Murudkar, S.; Mora, A. K.; Singh, P. K.; Nath, S. Origin of ultrafast excited state dynamics of 1-nitropyrene. *J. Phys. Chem*. A 2011, **115**(39), 10762–10766.

33 . Rawool, S. A.; Pai, M. R.; Banerjee, A. M.; Nath, S.; Bapat, R. D.; Sharma, R. K.; Jagannath; Dutta, B.; Hassan, P. A.; Tripathi, A. K. Superior interfacial contact yields efficient electron transfer rate and enhanced solar photocatalytic hydrogen generation in M/C3N4 Schottky junctions. ACS *Appl. Mater. Interfaces* 2023, *15*(33), 39926–39945.

34 . Malisa, S. C.; Raúl, G. B.; Gustavo, A. A. Quenching of I(2P½) by R-OH compounds. Influence of the alkyl group on the quenching efficiency. *Int. J. Chem. Kinet.* 1997, **29**(3), 155–160.

35 . Jimmy, M.; Kathrin, K.; Christopher, R.; Eric, V.; Mike, H.; Alexandre, F. Universal quenching of common fluorescent probes by water and alcohols. *Chem. Sci.* 2021, **12**, 1352–1362.

36 . Lei, W.; Boqiang, L.; Dionysios, D. D.; Baiyang, C.; Jie, Y.; Juan, L. Overlooked Formation of H2O2 during the Hydroxyl Radical-Scavenging Process When Using Alcohols as Scavengers. *Environ. Sci. Technol.* 2022, **56**(6), 3386–3396.

37 . Rachel, C. S.; Carsten, P.; David, L. S. The Role of Reactive Nitrogen Species in Sensitized Photolysis of Wastewater-Derived Trace Organic Contaminants. *Environ. Sci. Technol*. 2019, **53** (11), 6483–6491.

38 . Kimberly, M. P.; William, A. M. Halogen radicals contribute to photooxidation in coastal and estuarine waters. *Proc. Natl. Acad. Sci.* U. S. A. 2016, **113** (21), 5868–5873.